galaxies

MDPI

Article

Turning Galaxy Rotation Curves into Radial Cosmic Chronometers: A Nexus Paradigm Approach

Stuart Marongwe [1,*] and Stuart Allan Kauffman [2]

[1] Physics Department, University of Botswana, 4775 Notwane Road, Gaborone, Botswana
[2] Department of Biochemistry and Biophysics, University of Pennsylvania, 34th & Spruce Street, Philadelphia, PA 19104-6303, USA; stukauffman@gmail.com
* Correspondence: stuartmarongwe@gmail.com

Abstract

We present a novel method for deriving radially resolved dynamical chronometers from galaxy rotation curves, allowing galaxy assembly histories to be reconstructed directly from kinematic data. In the Nexus Paradigm, the baryonic Tully–Fisher relation is used to estimate the dynamical mass profile. We compare this profile with independently derived intrinsic baryonic mass distributions obtained from stellar Sérsic fits and gas surface-density measurement yields. This yields a radial ratio that maps to formation redshift with radial resolution. Inverting this ratio within a standard cosmological framework produces a radial lookback-time profile, representing the time since each radial shell last experienced dynamical reconfiguration. Applying the method to a pilot sample of seven SPARC galaxies, including both high- and low-surface-brightness systems as well as the Milky Way, reveals diverse age structures: stratified profiles associated with inside-out growth and flatter profiles consistent with coherent disk assembly. The method requires no dark-matter halo fitting and offers a kinematic chronometer that complements stellar population and chemical evolution approaches. The NP rotation-curve parameters were determined by minimizing the chi-squared statistic between the observed and predicted velocities using a two-stage optimization consisting of a global differential-evolution search followed by nonlinear least-squares refinement. Observational uncertainties were taken from the published rotation-curve data, supplemented by a 5 km s^{-1} systematic error floor added in quadrature to account for non-circular motions and other unresolved systematics. We also show that the governing dynamical equation admits a gravitoelectromagnetic interpretation, in which a velocity-dependent term generates disk-wide torques that regulate angular momentum transport. This leads to a unified stability framework in which galaxy morphology emerges from a single parameter regime: balanced conditions favor a coherent spiral structure, whereas dynamically hot regimes naturally produce diffuse and ultra-faint systems. The cosmological scaling of the effective gravitomagnetic field further suggests that the spiral structure is partly regulated by cosmic time. Although the inferred ages depend on the accuracy of the baryonic mass reconstruction and on the local validity of the evolving baryonic Tully–Fisher relation, our results show that rotation curves encode time-resolved dynamical information. This establishes the radial dynamical chronometer as a new observable for studying galaxy evolution and testing gravitational frameworks.

Keywords: galaxies evolution; galaxy kinematics and dynamics; high-redshift galaxies; alternative gravity theories

Check for updates

Academic Editor: Enrichetta Iodice

Received: 11 May 2026
Revised: 17 June 2026
Accepted: 22 June 2026
Published: 25 June 2026

Copyright: © 2026 by the authors. Licensee MDPI, Basel, Switzerland. This article is an open access article distributed under the terms and conditions of the Creative Commons Attribution (CC BY) license.

1. Introduction

Galaxy rotation curves have long been central to modern astrophysics. Since the pioneering spectroscopic observations of Andromeda by Rubin & Ford [1] and subsequent spiral-galaxy surveys [2], the approximately flat outer rotation velocities have been taken as evidence for unseen mass, usually attributed to extended dark-matter halos within the ΛCDM framework [3,4]. Despite its success in reproducing global dynamics, however, dark-matter-only modeling continues to face well-known challenges on galactic scales, including the too-big-to-fail and core–cusp problems [5,6].

An alternative empirical relation, the baryonic Tully–Fisher relation (BTFR), shows a remarkably tight correlation between rotation velocity and total baryonic mass (stars + gas) across six orders of magnitude in mass [7–9]. The Spitzer Photometry and Accurate Rotation Curves (SPARC) database, which contains 175 nearby disk galaxies with homogeneous 3.6 μm photometry and high-quality HI/Hα rotation curves, has established the BTFR as one of the most fundamental scaling relations in galaxy formation [8]. In the low-acceleration regime, the relation is also reproduced successfully by Modified Newtonian Dynamics [10–12], which introduces a universal acceleration scale below which Newtonian gravity is modified, removing the need for dark-matter halos.

Both ΛCDM halo models and standard MOND treat the BTFR as effectively time-independent at the present epoch. As a result, galaxy assembly histories are usually reconstructed only indirectly from stellar population synthesis [13,14], chemical evolution modeling, or morphological signatures of mergers and inflows [15]. Although these methods are informative, they do not provide a direct kinematic measure of when each radial shell last reached dynamical equilibrium.

The Nexus Paradigm of quantum gravity [16–19] offers a framework in which flat rotation curves emerge from a linearized spacetime metric without dark matter, while also predicting a cosmological evolution of the BTFR normalization. For a galaxy observed today, the dynamical mass inferred from the rotation curve is related to the intrinsic baryonic mass which is determined independently from photometry and gas maps through Equation (1). In a flat ΛCDM cosmology, the exponential factor reduces to a function of formation redshift, so the ratio between intrinsic and dynamical mass directly yields the lookback time since a radial shell last achieved virial equilibrium. In this way, the rotation curve can be recast as a radial cosmic chronometer, providing a direct map of assembly history across the disk.

$$M_{int}(r) = M_{dyn}(r) \times e^{-4\int_{t_{form}}^{t_0} H(t)\, dt}, \tag{1}$$

where $M_{dyn}(r) = v_{obs}(r)^4/(Ga_0)$ with $a_0 = H_0 c/(2\pi)$. In a flat ΛCDM cosmology, this exponential factor becomes $(1 + z_{\text{form}})$, so the ratio $M_{int}(r)/M_{dyn}(r)$ directly yields the lookback time since the radial shell last achieved virial equilibrium. Thus, the radial cosmic chronometer is a method that transforms galaxy rotation curves into spatially resolved estimates of dynamical assembly age, providing a radial map of the time elapsed since the last major virialization event within a galaxy.

This study develops the methodology and applies it to an expanded SPARC sample spanning both high-surface-brightness (HSB) and low-surface-brightness (LSB) galaxies. We also incorporate Monte Carlo error propagation and adopt the Planck 2018 cosmological parameters [20]. The resulting chronometer reveals distinct assembly modes and offers a new way to probe galaxy evolution without relying on dark-matter halo fitting.

A longstanding question in extragalactic astrophysics is why the BTFR is so tight for disk galaxies while pressure-supported systems such as dwarf spheroidals and galaxy clusters show systematic offsets. These deviations are often attributed to baryonic physics

or dark-matter halo diversity. Here, we argue instead that they reflect a deeper feature of galaxy evolution: the BTFR is not a single static law, but the present-day projection of an underlying time-dependent scaling relation. In this picture, dynamically young galaxies cluster near the current normalization and therefore define a tight relation with little scatter, whereas dynamically older systems formed at higher redshift naturally occupy offset tracks because the normalization evolves with time [18,19]. This interpretation recasts scatter in galaxy scaling relations as a physically meaningful signal of formation epoch and dynamical history, rather than as mere residual noise.

Another longstanding question is how different galaxy morphologies arise and evolve over cosmic time. In particular, it remains unclear why some galaxies develop a strong spiral structure, bars, and active star-forming disks, whereas others remain diffuse, weakly structured, and dynamically quiescent despite occupying similar large-scale environments. Addressing this problem requires a quantitative measure of galactic stability that connects the observed kinematics of a galaxy to its evolutionary state.

In this work we introduce the gravitoelectromagnetic stability parameter, Q_{GEM}, defined as $Q_{\mathrm{GEM}} \equiv \frac{c_s\,\kappa_{\mathrm{eff}}}{\pi G \Sigma_0}$ where c_s is the characteristic gas velocity dispersion, Σ_0 is the baryonic surface density, and κ_{eff} is the gravitoelectromagnetically modified epicyclic frequency. Q_{GEM} is a dimensionless measure of the dynamical state of a galactic disk that quantifies the competition between stabilizing rotational support and destabilizing self-gravity. Systems with $Q_{\mathrm{GEM}} < 1$ are dynamically unstable and prone to vigorous structural evolution and enhanced star formation, $Q_{\mathrm{GEM}} \approx 1$ corresponds to marginally stable spiral disks, while $Q_{\mathrm{GEM}} > 1$ characterizes increasingly stable and diffuse systems in which the growth of large-scale structure is suppressed.

The introduction of Q_{GEM} provides a direct physical link between galaxy morphology, disk stability, and the radial cosmic chronometer developed in this work. Together, these quantities allow present-day rotation curves to be interpreted not only as tracers of mass distribution but also as indicators of the dynamical assembly history and evolutionary state of galaxies.

Recent studies have shown that galaxy kinematics are influenced by both internal and environmental processes. Magnetohydrodynamic simulations and observations have revealed correlations between large-scale magnetic-field strength, rotational velocity, and dynamical mass in disk galaxies, highlighting a close connection between galactic dynamics and structural evolution [21,22]. In addition, investigations of brightest group galaxies have demonstrated that the dynamical state of the surrounding environment can significantly affect stellar and gas kinematics, with dynamically disturbed systems exhibiting signatures distinct from those of relaxed groups [23]. These findings suggest that galaxy rotation curves encode information not only about the present mass distribution but also about the cumulative dynamical history of the system, motivating the search for observational diagnostics capable of tracing galaxy assembly and evolution.

2. Theoretical Framework

2.1. A Semi-Classical Derivation of Quantum Gravity

We initiate the search for a quantum theory of gravity by adopting an intrinsic-geometric interpretation of Einstein's field equations, treating these equations as describing curved worldlines embedded within a flat spacetime manifold. This perspective offers an alternative pathway to quantum gravity, since quantum field theory is conventionally formulated on flat spacetime backgrounds and represents curved trajectories through Feynman's sum-over-histories formulation. The Ricci curvature tensor in Einstein's field equations can be interpreted as encoding the statistical average of possible trajectories that a test particle may follow under the influence of a gravitational field. Given two vector

fields X and Z, the Ricci tensor satisfies $Ric(X,Z) = \sum_i^n \langle R(X,e_i)Z,e_i\rangle = -\frac{1}{2}\Delta g_{ij}$. Hamilton's viewpoint is analogous to thermal diffusion and offers an intuitive framework in which Hamilton's Ricci Flow plays a central role in formulating quantum gravity. The next section introduces Ricci Flow and its basic properties, which are essential to developing a self-consistent model of quantum gravity.

2.1.1. Hamilton's Ricci Flow

In 1982, Richard Hamilton introduced the Ricci Flow as a geometric evolution equation [23]. On a Riemannian manifold, the Ricci Flow is a partial differential equation governing the deformation of the metric tensor:

$$\partial_t g_{\mu\nu} = -2Ric\big(g_{\mu\nu}(t)\big) \tag{2}$$

where $Ric\big(g_{\mu\nu}(t)\big)$ denotes the Ricci curvature of the metric $g_{\mu\nu}(t)$. The time evolution of the metric under the Ricci Flow spreads the curvature evenly through space.

For compact Einstein manifolds, the Ricci Flow is expressed as follows:

$$\partial_t g_{\mu\nu} = -\frac{cr_H}{3} G_{\mu\nu} \tag{3}$$

where $G_{\mu\nu} = R_{\mu\nu} - \frac{1}{2}Rg_{\mu\nu}$ is the Einstein tensor, c the speed of light and r_H the Hubble radius. Compact Einstein manifolds satisfy

$$G_{\mu\nu} = kg_{\mu\nu} \tag{4}$$

In GR with the cosmological constant Λ, the compact Einstein manifold takes the form

$$G_{\mu\nu} = \Lambda g_{\mu\nu} \tag{5}$$

This suggests that vacuum solutions to Einstein's field equations are compact Einstein manifolds with k proportional to the cosmological constant. The above equation describes a Ricci soliton of de Sitter topology and is divergenceless. That is, $\nabla_\mu G_{\mu\nu} = \Lambda\nabla_\mu g_{\mu\nu} = \kappa\rho_{DE}\nabla_\mu g_{\mu\nu} = 0$ where κ is the Einstein constant and ρ_{DE} is the dark-energy density. This configuration represents a localized packet of vacuum energy in the form of a Ricci soliton, within which energy conservation is strictly maintained. In other words, the Ricci soliton constitutes a self-gravitating gravitational field.

2.1.2. Spacetime Quantization

In the Nexus Paradigm of quantum gravity, we initiate the quantization procedure by considering a finite patch of Minkowski space equipped with a non-degenerate, symmetric, bilinear form on the tangent space. We adopt a local coordinate system to circumvent the necessity of an origin and to avoid point-like events, which are sources of divergences in quantum field theory. This local coordinate formulation renders Minkowski space a displacement vector space. The inner product is consequently given by

$$\begin{aligned} \Delta s^2 = \Delta x^\mu \Delta x_\mu = \Delta x^2 + \Delta y^2 + \Delta z^2 - c^2\Delta t^2 \\ = (A\Delta x + B\Delta y + C\Delta z + icD\Delta t)(A\Delta x + B\Delta y + C\Delta z + icD\Delta t) \end{aligned} \tag{6}$$

Upon multiplication of the right-hand side, cancelation of all cross terms such as $\Delta x\Delta y$ requires

$$AB + BA = 0, \cdots \text{and } A^2 = B^2 = \cdots = 1 \tag{7}$$

These conditions generate a Clifford algebra, implying that the coefficients (A, B, C, D) must be matrices, specifically the Dirac gamma matrices. These matrices are square roots of the Minkowski metric:

$$\boldsymbol{I}_4 \gamma^\mu \gamma^\nu = \eta^{\mu\nu} \tag{8}$$

Thus, the displacement vectors $\Delta x^\mu = a\gamma^\mu$ reside in Clifford space $Cl_{1,3}(R)_C$ implying an intrinsic quantized spin and can be perceived as Dirac 4-vector matrices analogous to the Pauli vector matrices in three dimensions. They are also quantized wave packets or pulses of spacetime that can be expressed as Fourier integrals as follows

$$\begin{array}{c} \Delta x_n^\mu = \frac{2r_{HS}}{n\pi} \gamma^\mu \int_{-\infty}^{\infty} sinc(kx) e^{ikx} dk \\ = \gamma^\mu \int_{-\infty}^{\infty} a_{nk} \varphi_{(nk)} dk \end{array} \tag{9}$$

where

$$\frac{2r_{HS}}{n\pi} = \sum_{k=-\infty}^{k=+\infty} a_{nk} \tag{10}$$

Here r_{HS} is the Hubble radius, $\varphi_{(nk)} = sinc(kx)e^{ikx}$ are Bloch energy eigenstate functions in which the four wave vectors assume the following quantized values:

$$k^\mu = \frac{n\pi}{r_{HS}^\mu} \; n = \; \pm 1, \pm 2 \ldots 10^{60} \tag{11}$$

We impose a high-energy cutoff at the Planck four-length, as no measurement can be obtained below this scale without black hole formation, and a low-energy cutoff at the Hubble four-radius, since no information can be retrieved beyond the cosmic horizon. The 10^{60} states arise from the ratio of the Hubble four-radius to the Planck four-length. The Bloch functions in each eigenstate of spacetime generate an infinite Bravais four lattice. The conjugate momentum for the displacement vectors is

$$\begin{array}{c} \Delta p_n^\mu = \frac{2np_1}{\pi} \gamma^\mu \int_{-\infty}^{\infty} \varphi(kx) dx \\ = \gamma^\mu \int_{-\infty}^{\infty} c_n \varphi(kx) dx \end{array} \tag{12}$$

where p_1 is the four-momentum of the ground state.

The wave packet may be interpreted as a particle of four-space and can be envisioned as enveloping a spherically symmetric concentration of an excited energy state of the quantum vacuum.

We now seek to establish the relationship between these spacetime wave packets and the Ricci solitons of Equation (5). First, we determine the norm squared of the four-momentum for the n-th state wave packet. This norm is computed by multiplying the inner product of Equation (11) by the square of the reduced Planck constant:

$$(\hbar)^2 k^\mu k_\mu = \frac{E_n^2}{c^2} - \frac{3(nhH_0)^2}{c^2} = 0 \tag{13}$$

where H_0 is the Hubble constant. We then express Equation (13) in terms of the cosmological constant, Λ, as

$$\Lambda_n = \frac{E_n^2}{(hc)^2} = \frac{3k_n^2}{(2\pi)^2} = n^2 \Lambda \tag{14}$$

From Equation (13), the wave packet can be considered as a compact Einstein manifold or a trivial Ricci soliton of positive Ricci curvature expressed in the form

$$G_{(nk)\mu\nu} = n^2 \Lambda g_{(n,k)\mu\nu} = n^2 \kappa \rho_\Lambda g_{(n,k)\mu\nu} \tag{15}$$

Clearly Equation (15) depicts a self-gravitating Ricci soliton and as explained in Ref. [16] this is dark matter (DM) which is a localized packet of vacuum energy $n^2\rho_\Lambda$ in the n-th quantum state. Thus, DM is a Ricci soliton and should exhibit the following soliton characteristics:

1. It is a localized lump of vacuum energy;
2. It preserves its form while growing or diminishing in size;
3. It preserves its speed and form after colliding with another soliton.

The lowest quantum state from Equation (11) occurs when $n = 1$ suggesting that for Equation (15) to become Ricci flat in this state, a Ricci soliton in the ground state must be removed from the right side yielding Einstein's vacuum field equations in the quantized spacetime as

$$G_{(nk)\mu v} = \left(n^2 - 1\right)\Lambda g_{(n,k)\mu v} = \left(n^2 - 1\right)k\rho_\Lambda g_{(n,k)\mu v} \tag{16}$$

Equation (16) describes a decay mechanism in which a high-energy graviton emits a ground-state graviton to transition to a lower quantum state. The force generated by this emission process may be computed via the uncertainty principle. We consider the ground-state graviton as possessing a temporal interval Δx equal to the Hubble radius.

Thus, $\Delta t \Delta E = \Delta t \Delta x \cdot F = \frac{cF}{H_0^2} \sim \frac{h}{2\pi}$.

Therefore

$$F \sim \frac{hH_0}{c^2} \cdot \frac{H_0 c}{2\pi} = m_G \cdot a \tag{17}$$

This implies that the mass of the ground-state Ricci soliton/graviton is $m_G = \frac{hH_0}{c^2}$ which in 3D space is $m_G = \frac{3hH_0}{c^2}$ and the graviton-induced acceleration is $a = \frac{H_0 c}{2\pi}$. Thus, a spherical volume of space containing a dark-energy mass $M_\Lambda(r)$ within a radius r will always generate a scale-invariant outward acceleration of $\frac{GM_\Lambda(r)}{r^2} = -\frac{H_0 c}{2\pi}$. This acceleration was first empirically observed by Milgrom from data on galaxy rotation curves [24]. As noted by Milgrom, non-Newtonian dynamics begins to manifest at this critical acceleration. This critical acceleration therefore marks a transition from the classical to the quantum gravity regime.

The framework distinguishes two classes of solitons: vacuum de Sitter solitons with quantum states $n^2 = \frac{r_H^2}{r_n^2}$, where r_H is the Hubble radius; and anti-de Sitter (AdS) solitons with quantum states $^2 = \frac{r_n c^2}{GM(r)}$, which are associated with baryonic matter. In a vacuum, spacetime constitutes a dS Ricci soliton field with energies spanning the Planck scale to the Hubble scale. The energy eigenstates arise from the Heisenberg Uncertainty Principle $\Delta E_n \cdot \Delta r_n \sim \hbar$. Ref. [16] explains why the high energy states cancel out, leaving a Higgs-like ground state which manifests itself as dark energy. Dark matter in this framework is therefore an excited dS Ricci soliton state of vacuum energy ΔE_n and radius r_n.

Spacetime in the presence of baryonic matter is described in terms of de Sitter and anti-de Sitter solitons, together with a ground-state de Sitter soliton that represents dark energy. This structure is expressed by Equation (18).

$$G_{(nk)\mu v} = (\tilde{n}^2 + n^2 - 1)\Lambda g_{(nk)\mu v} \tag{18}$$

Einstein's field equations are written here in purely geometric form, describing a compact Einstein manifold which is maximally symmetric. For any quantum state in which a Ricci soliton has constant curvature, energy is conserved [16]. In this interpretation, the right-hand side represents the quantum or energetic state of spacetime, whereas the left-hand side acts as a Laplacian-like operator that averages the trajectory of a test particle in the corresponding gravitational field.

The linearized form of Equation (18) can be represented as a Ricci soliton in the N-th quantum state, leading to Equation (19).

$$G_{(Nk)\mu v} = N^2 \Lambda g_{(Nk)\mu v} \tag{19}$$

2.2. Derivation of the Evolving BTFR

Following [16], the exact solution of Equation (19) leads to the metric form shown in Equation (20).

$$\begin{aligned} ds^2 &= -\left(1-\left(\tfrac{2}{N^2}\right)\right)c^2dt^2 + \left(1-\left(\tfrac{2}{N^2}\right)\right)^{-1}dr^2 + r^2\left(d\theta^2 + sin^2\theta d\varphi^2\right) \\ &= -\left(1-\left(\tfrac{2GM_N}{rc^2}\right)\right)c^2dt^2 + \left(1-\left(\tfrac{2GM_N}{rc^2}\right)\right)^{-1}dr^2 + r^2\left(d\theta^2 + sin^2\theta d\varphi^2\right) \end{aligned} \tag{20}$$

Here, $M_N(r) = M_B(r) + M_{DM}(r) + M_\Lambda(r)$, where the terms on the right denote the baryonic mass, dark-matter mass, and dark-energy mass enclosed within a sphere of radius r. Equation (20) is an exterior Schwarzschild solution to a dS Ricci soliton with baryonic matter and an excited vacuum energy state embedded within it. The mass decomposition leads directly to the metric equation given in Equation (21).

$$ds^2 = -\left(1-2\left(\frac{GM_{int}}{rc^2} + \frac{Hvr}{c^2} - \frac{H_0cr}{2\pi c^2}\right)\right)c^2dt^2 + \left(1-2\left(\frac{GM_{int}}{rc^2} + \frac{Hvr}{c^2} - \frac{H_0cr}{2\pi c^2}\right)\right)^{-1}dr^2 + r^2\left(d\theta^2 + sin^2\theta d\varphi^2\right) \tag{21}$$

In this metric, $\frac{GM_{DM}(r)}{r} = v^2 = (Hr)^2 = Hvr$ and $\frac{GM_\Lambda(r)}{r} = -\frac{H_0cr}{2\pi}$ with M_{int} as the intrinsic baryonic mass. Substituting these relations yields the gravitational equation in Equation (22).

$$\frac{d^2r}{dt^2} = \frac{GM_{int}}{r^2} + Hv - \frac{H_0c}{2\pi} \tag{22}$$

Equation (22) describes Newtonian/Einsteinian gravity within a rotating and expanding compact Einstein manifold, or Ricci soliton. Equation (21) can be interpreted as a boundary solution of a dS Ricci soliton of radius r, with baryonic matter and an excited vacuum energy state embedded within it. Here, H is the Hubble parameter associated with the local compact Einstein manifold of the galaxy, whereas H_0 is the Hubble parameter of the ground-state, or background, Ricci soliton. Beyond the boundary, the dS Ricci soliton behaves as an AdS soliton and interacts with other excited vacuum soliton states via Newtonian/Einsteinian gravity. This boundary solution is the nexus of AdS-dS correspondence.

Galactic dynamics enters the non-Newtonian regime when the Newtonian term is exactly balanced by the expansion, or dark-energy, term.

$$\frac{GM_{int}(r)}{r^2} = \frac{H_0}{2\pi}c = \frac{v^2}{r} \tag{23}$$

Under this condition, the characteristic radius is given by

$$r = \frac{2\pi v^2}{H_0 c} \tag{24}$$

Substituting for r into Equation (23) yields the baryonic Tully–Fisher relation.

$$v^4 = GM_{int}(r)\frac{H_0}{2\pi}c \tag{25}$$

The equilibrium condition of Equation (23) reduces Equation (22) to Equation (26).

$$\frac{d^2r}{dt^2} = \frac{dv}{dt} = Hv \tag{26}$$

From which we obtain the following equations of galactic and cosmic evolution

$$r = \frac{1}{H}e^{(Ht)}(GM_{int}(r)\frac{H_0}{2\pi}c)^{\frac{1}{4}} = \frac{v}{H} \tag{27}$$

$$v = e^{(Ht)}(GM_{int}(r)\frac{H_0}{2\pi}c)^{\frac{1}{4}} = Hr \tag{28}$$

$$a = He^{(Ht)}(GM_{int}\frac{H_0}{2\pi}c)^{\frac{1}{4}} = Hv \tag{29}$$

Rearranging Equation (28) for the baryonic mass gives the form used for empirical comparisons, shown in Equation (30).

$$M_{int} \propto e^{-4Ht}v^4. \tag{30}$$

This derivation highlights two central features of the evolving BTFR: first, an invariant slope of 4, which reflects the underlying gravitational equilibrium between baryons and dark-matter halos which are interpreted in the Nexus Paradigm as Ricci solitons in quantized spacetime; and second, a time-dependent normalization, which captures the dilution of vacuum-energy localization over cosmic history. Together, these features provide the basis for the observed tightness of the BTFR across diverse galaxy populations.

2.3. Refinement with Time-Varying Hubble Parameter

A more accurate formulation replaces the parameter H with the time-varying Hubble parameter $H(t) = \dot{a}(t)/a(t)$ for the expansion rate of the Ricci soliton and integrating its effect over the galaxy's lifetime:

$$M_{int} \propto e^{-4\int_{t_{\text{form}}}^{t_0} H(t)dt}v^4 \tag{31}$$

This refinement accounts for the faster expansion rate in the early universe. In a flat ΛCDM cosmology with $H_0 = 67.15$ km/s/Mpc, $\Omega_m = 0.315$, and $\Omega_\Lambda = 0.685$ from [20] the Hubble parameter evolves as:

$$H(z) = H_0\sqrt{\Omega_m(1+z)^3 + \Omega_\Lambda} \tag{32}$$

The integral $\int H(t)dt$ can be evaluated using the relation $dt = dz/((1+z)H(z))$, yielding $\int Hdt = \ln(1+z)$. This simplification greatly facilitates practical calculations.

2.4. Cosmological Lookback Time

In a flat ΛCDM universe with $H(z) = H_0\sqrt{\Omega_m(1+z)^3 + \Omega_\Lambda}$, $\int_{t_{\text{form}}}^{t_0} Hdt = \ln(1+z_{\text{form}})$. Thus, from (1),

$$1 + z_{\text{form}}(r) = \left(\frac{M_{\text{dyn}}(r)}{M_{\text{int}}(r)}\right)^{\frac{1}{4}}, \tag{33}$$

The lookback time $t_{\text{lb}}(r) = t_0 - t(z_{\text{form}})$ is obtained by inverting the age–redshift relation of the chosen cosmology [20]. It is important to note that the dynamical age computed from Equation (33) measures the time since the last violent disturbance that

disrupted virial equilibrium—not the age of the stars. Virialization is established when the condition described by Equation (23) is satisfied.

3. Materials and Methods

3.1. Observational Inputs

For each galaxy we require:

- Rotation curve $v_{\rm obs}(r)$ with uncertainties [8].
- Intrinsic baryonic mass profile $M_{\rm int}(r) = M_*(r) + M_{\rm gas}(r)$, derived independently from:
  - Stellar mass profile: Sérsic fit to surface brightness, multiplied by a mass-to-light ratio from stellar population synthesis.
  - Gas mass profile: HI (and H_2) surface-density map, integrated to obtain the enclosed gas mass.

Sample Selection Criteria

The galaxy sample was selected from the SPARC database to provide a representative comparison between high-surface-brightness (HSB) and low-surface-brightness (LSB) systems while ensuring sufficient data quality for reliable chronometer reconstruction.

The selection was based on the following criteria:

1. *High-quality rotation curves:* Galaxies were required to possess well-sampled rotation curves extending over a substantial fraction of the optical disk with published velocity uncertainties.
2. *Reliable photometric decompositions:* Surface-brightness profiles and baryonic mass models had to be available in the SPARC archive in order to compute the luminosity-coupled core-radius evolution and the gravitoelectromagnetic stability parameter.
3. *Coverage of distinct dynamical regimes:* The sample was chosen to include both HSB and LSB galaxies spanning a range of morphologies, from strongly structured spiral systems to diffuse low-density disks.
4. *Minimal evidence for severe disturbance:* Galaxies undergoing major mergers or exhibiting strongly disrupted kinematics were excluded to ensure that the inferred radial chronometer primarily traces secular dynamical evolution.

The final sample consists of four HSB galaxies (NGC 2841, NGC 2903, NGC 3198, and NGC 2403) and three LSB galaxies (UGC 128, UGC 191, and F568-3). These systems were selected because they have been extensively studied, possess high-quality rotation curves, and collectively span a broad range of surface brightness, mass, and dynamical structure.

Although the sample is not intended to be statistically complete, it provides a useful benchmark for testing whether the radial cosmic chronometer and the gravitoelectromagnetic stability parameter can distinguish between dynamically evolved spiral galaxies and diffuse low-density systems.

Table 1 contains quantities obtained directly from the SPARC database, including distances, radial coverage, and rotation-curve sampling.

Table 1. Observational properties of the galaxy sample (SPARC).

Galaxy	Type	Distance (Mpc)	r_{max} (kpc)	N Rotation-Curve Points	$V_{max,obs}$ (km s^{-1})
NGC 2841	HSB	14.1	63.64	50	323
NGC 2903	HSB	6.6	24.96	34	216
NGC 3198	HSB	13.8	44.08	43	157

Table 1. *Cont.*

Galaxy	Type	Distance (Mpc)	r_{max} (kpc)	N Rotation-Curve Points	$V_{max,obs}$ (km s^{-1})
NGC 2403	HSB	3.16	20.87	73	136
UGC 128	LSB	64.5	53.75	22	134
UGC 191	LSB	17.1	9.98	9	83.8
F568-3	LSB	82.4	17.98	18	120

Notes: Distances, radial extents, and rotation-curve measurements are taken directly from the SPARC archive. $V_{max,obs}$ denotes the maximum observed rotation velocity.

3.2. Derivation of $M_{dyn}(r)$

In the Nexus Paradigm, the enclosed dynamical mass profile for galaxies takes the form (with $\beta = 1$ for HSB galaxies and $\beta = 2$ for LSB galaxies)

$$M_{\rm dyn}(r) = M_{\rm total}\left(\frac{r}{r_c(r)+r}\right)^{3\beta}, \tag{34}$$

where $r_c(r) = r_{c0}[1 + \eta f_{\rm norm}(r)^{\alpha}]$ and $f_{\rm norm}(r)^{\alpha}$ is the luminosity fraction from a Sérsic profile. The rotation curve is given by

$$v(r) = (G\, M_{\rm dyn}(r)\, a_0)^{\frac{1}{4}},\ a_0 = \frac{H_0 c}{2\pi}, \tag{35}$$

Equation (35) can be simplified to

$$v(r) = v_{max}\left(\frac{r}{r_c(r)+r}\right)^{3\beta/4} \tag{36}$$

A sample of 10 HSB and 10 LSB galaxies is used in Appendix A to demonstrate the excellent agreement of Equation (36) with observations. In Appendix B, we make a benchmark comparison with standard rotation-curve models such as MOND, NFW Halo, Burket Halo Arctan ($\alpha = 1$) and Arctan ($\alpha = 1/2$). We compare these models using AIC, BIC, χ^2 and χ^2_ν statistics from a sample 165 SPARC galaxies.

3.3. Ratio and Lookback Time

Compute the radial ratio

$$R(r) = \frac{M_{\rm dyn}(r)}{M_{\rm int}(r)}. \tag{37}$$

Insert into (33) to obtain $z_{\rm form}(r)$. Convert to lookback time using the standard cosmological model. The resulting $t_{\rm lb}(r)$ is the time elapsed since the material at radius r last participated in a virialization event (i.e., since the dynamical clock was reset). The computation is only valid where $M_{\rm dyn}/M_{\rm int} > 1$, i.e., when condition (23) is satisfied.

3.4. Uncertainties

Uncertainties in $v_{\rm obs}$ and in the stellar/gas mass profiles propagate into $R(r)$. A Monte Carlo approach is used to estimate the error bars on $t_{\rm lb}(r)$.

4. Results: Radial Assembly Histories from Sérsic-Coupled Radial Chronometers

The Sérsic-optimized Nexus Paradigm (NP) framework enables a direct inversion of galaxy rotation curves into radial dynamical histories, providing a kinematic probe of galaxy

formation that is independent of stellar population modeling. Figures 1 and 2 demonstrate that the combination of (i) the NP kinematic relation and (ii) a Sérsic-coupled core scale,

$$r_c(r) = r_{c0}[1 + \eta f_{\rm norm}(r)^{\alpha}], \tag{38}$$

yields robust reconstructions of both rotation curves and the associated radial chronometer,

$$1 + z_{\rm form}(r) = \left(\frac{M_{\rm dyn}}{M_{\rm int}}\right)^{1/4}. \tag{39}$$

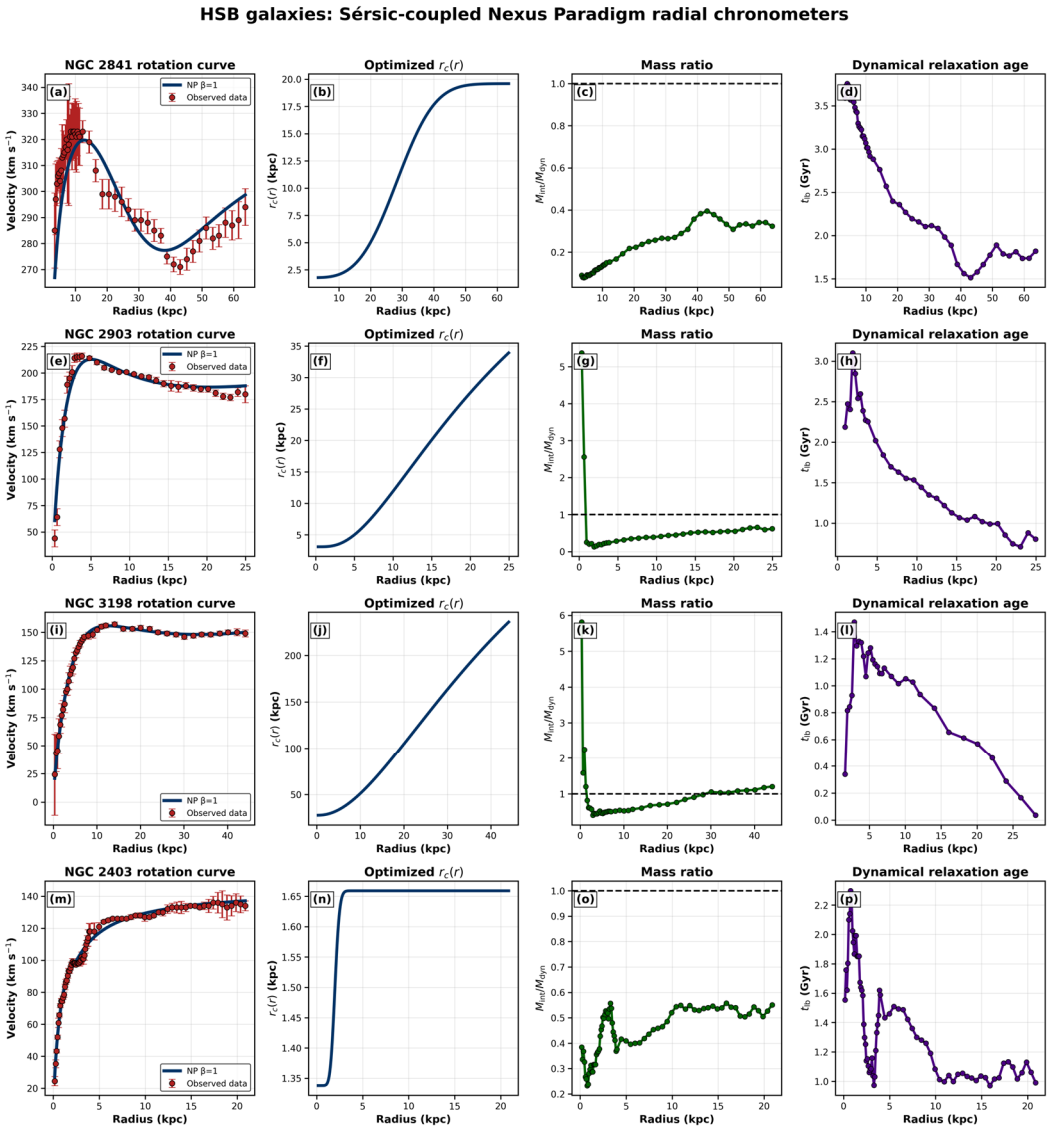


Figure 1. Radial cosmic chronometer reconstruction for high-surface-brightness galaxies within the Nexus Paradigm.

The resulting profiles reveal a systematic mapping between galaxy structure and assembly history, which we analyze below.

4.1. High-Surface-Brightness Galaxies: Stratified Assembly and Dynamical Differentiation

The figure presents, for each galaxy, (left to right) the observed rotation curve with model fit, the Sérsic-coupled core scale $r_c(r)$, the mass ratio $M_{\rm int}/M_{\rm dyn}$, and the derived dynamical age profile $t_{\rm lb}(r)$. High-surface-brightness (HSB) galaxies exhibit pronounced

negative age gradients, indicative of temporally stratified, inside-out assembly. The close agreement between the reconstructed rotation curves and observations demonstrates that the Sérsic-optimized Nexus Paradigm framework simultaneously captures galaxy kinematics and encodes their radial assembly histories. The HSB galaxies exhibit strong radial gradients in the inferred dynamical age $t_{\rm lb}(r)$, indicating significant temporal stratification.

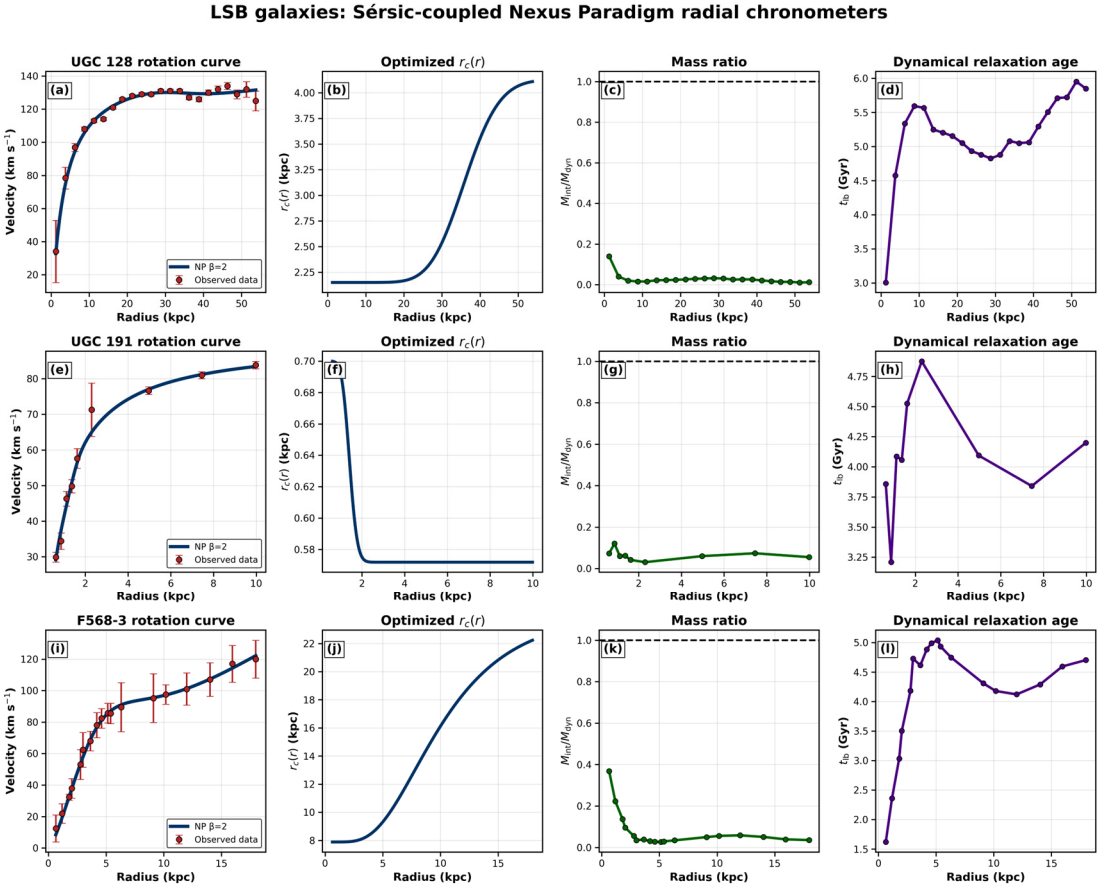


Figure 2. Radial cosmic chronometer reconstruction for low-surface-brightness (LSB) galaxies within the Nexus Paradigm.

NGC 2841: canonical inside-out growth

NGC 2841 displays the steepest radial gradient in the sample, with $t_{\rm lb}(r)$ decreasing from $\sim$ 4.0 Gyr in the central regions to $\sim$ 2.0 Gyr in the outer disk. The corresponding mass-ratio profile is smooth and monotonic, remaining well below unity across all radii, indicating a dynamically relaxed system.

This behavior is characteristic of inside-out assembly, where the central regions formed during an early, high-density phase, and subsequent disk growth occurred through extended accretion. The absence of discontinuities in both $M_{\rm int}/M_{\rm dyn}$ and $t_{\rm lb}(r)$ suggests that this process was continuous rather than merger-dominated, consistent with a dissipative collapse followed by gradual disk buildup.

NGC 2903: secular evolution in a barred disk

NGC 2903 exhibits a smooth radial decline in $t_{\rm lb}(r)$ from $\sim$ 3 Gyr to $\sim$ 1 Gyr, but with mild irregularities in the inner mass-ratio profile. These deviations coincide with the known presence of a bar, which induces non-axisymmetric flows.

The inferred history indicates an initially established disk, followed by secular redistribution of mass and angular momentum. Unlike NGC 2841, the gradient is shallower and more continuous, reflecting internal evolution rather than hierarchical assembly.

NGC 3198: coeval disk formation

NGC 3198 shows an approximately flat age profile, $t_{\rm lb}(r) \sim 2.4$–0.2 Gyr across all radii. The mass ratio is correspondingly uniform, and the rotation curve is reproduced with minimal residuals.

This behavior implies that the disk formed as a single dynamical unit, with negligible radial differentiation in formation time. Such coeval formation is indicative of smooth gas accretion and the absence of strong early collapse or merger events. This system represents a limiting case in which the NP chronometer reduces to a global formation epoch.

NGC 2403: weak inside-out growth

NGC 2403 displays a shallow radial gradient, with $t_{\rm lb}(r)$ decreasing from ~ 2.5 Gyr to ~ 1 Gyr. Both the rotation curve and mass-ratio profile are smooth and featureless.

This behavior indicates a low-intensity inside-out assembly process dominated by quiescent star formation and gradual accretion. The absence of strong gradients or irregularities suggests a dynamically stable evolutionary history.

4.2. Physical Implications

These results demonstrate that galaxy rotation curves contain sufficient information to reconstruct the formation epoch as a function of radius, assembly mode (hierarchical vs. quiescent), and dynamical relaxation history, without recourse to stellar population synthesis or chemical evolution models.

In this framework, rotation curves are elevated from static tracers of mass distribution to time-resolved dynamical observables, providing a new pathway for probing galaxy formation and testing gravitational physics.

5. Methodology for LSB Galaxies

For each galaxy, the panels show (left to right) the observed rotation curve with model fit, the Sérsic-coupled core scale $r_c(r)$, the mass ratio $M_{\rm int}/M_{\rm dyn}$, and the inferred dynamical age profile $t_{\rm lb}(r)$. The LSB systems exhibit slowly rising rotation curves, consistently low mass ratios, and shallow dynamical-age gradients, indicating diffuse gravitational collapse and temporally extended, quasi-coherent assembly. Compared to HSB galaxies, the reduced magnitude of $dt_{\rm lb}/dr$ reflects weaker radial differentiation and the absence of strong merger-driven restructuring, supporting a picture of long-timescale evolution dominated by steady gas accretion and low star-formation efficiency.

In the Nexus Paradigm, the enclosed baryonic mass profile for LSB galaxies takes the form of Equation (36) with $\beta = 2$.

$$M_{\rm int}(r) = M_{\rm total}\left(\frac{r}{r_c(r)+r}\right)^6, \tag{40}$$

where $r_c(r) = r_{c0}[1+\eta f_{\rm norm}(r)^\alpha]$ and $f_{\rm norm}(r)^\alpha$ is the luminosity fraction from a Sérsic profile. The rotation curve is given by Equation (36).

For LSB galaxies, the intrinsic baryonic mass $M_{\rm int}(r)$ is often dominated by gas, and the stellar component has a very low surface brightness. The dynamical age $t_{\rm lb}(r)$ is extracted by comparing the observed rotation curve with an independently derived intrinsic mass profile.

The rotation curve rises slowly (typical for LSB galaxies) and flattens at ≈66 km/s. The dynamical age gradient (∼5 Gyr in the center, ∼2.5 Gyr in the outskirts) suggests an inside-out assembly, but with a much lower age contrast than HSB galaxies.

UGC 128 Extended slow assembly (diffuse system)

Observed Signatures

- Rotation: Exhibits a notably gradual increase;
- Mass Ratio: Extremely low;

- Age: Characterized by a broad, shallow profile.

Radial History

- Inner Region: Moderately old stellar population, but not exceptionally so;
- Outer Region: Slightly younger relative to the Inner Region.

Interpretation

- Indicates diffuse gravitational collapse;
- The weak gravitational potential suggests slow evolutionary processes;
- No evidence for a distinct early epoch of development.

UGC 191 Compact LSB Galaxy with Mild Gradient
Observed Signatures

- Rotation: Displays a moderate rise;
- Mass ratio: Low, though marginally higher than UGC 128;
- Age: Reveals a weak gradient.

Radial History

- Inner Region: Contains a somewhat older core;
- Outer Region: Younger, though the age difference is not substantial.

Interpretation

- Represents a transitional system exhibiting characteristics between:
- Pure LSB galaxies (e.g., UGC 128);
- Systems with mild high surface brightness (HSB)-like attributes.

F568-3 Extended Disk with Gradual Evolution
Observed Signatures

- Rotation: Smooth, continuous increase;
- Mass ratio: Consistently low across the disk;
- Age: Shallow gradient observed.

Radial History

- **Entire Disk:** Undergoes slow, continuous formation without abrupt changes.

Interpretation

- Suggests long-timescale assembly;
- Likely influenced primarily by:
- Steady gas inflow;
- Low star formation efficiency.

Cross-Validation with the Literature

The literature on LSB galaxies provides several independent constraints:

- Star formation histories—Van den Hoek et al. [25] found that LSB galaxies have evolved slowly, with present-day gas fractions ∼0.5 and ages up to 14 Gyr. They also noted that LSB galaxies contain old stellar populations, implying they did not form late.
- Minimum ages—Vorobyov et al. [26] estimated that the age of blue LSB galaxies may vary between 1.5 and 6 Gyr and 13 Gyr, depending on the physical conditions in the disk. Their models suggested a tentative minimum age of 1.5–3 Gyr from colors and oxygen abundances, but larger values (5–6 Gyr) from H equivalent widths.
- Stellar masses—Du et al. [27] derived stellar masses for LSB galaxies spanning log $M^*/M_\odot$ = 7.1–11.1, with a mean of 8.5, lower than normal galaxies.

- UGC 1281—This galaxy is a slightly warped, edge-on dwarf LSB with a red stellar thick disk. Its rotation curve is well resolved and shows a slow rise.

Our derived dynamical age for UGC 1281 (∼4 Gyr mean, with a central age of ∼5 Gyr) falls within the 1.5–6 Gyr range quoted by Vorobyov et al. The central region is older, consistent with the presence of an old stellar population noted by [25]. The outer, younger age (∼2.5 Gyr) aligns with the idea that LSB galaxies have experienced slow, inside-out growth without a recent major merger. LSB galaxies are relatively undisturbed galaxies compared to HSBs. Because LSB galaxies are dynamically quieter and less frequently reset than HSB systems, the radial chronometer is expected to correlate more strongly with chemical gradients in LSB galaxies. Using the observed LSB chronometer gradients, a monotonic sequence of weak metallicity gradients would yield Pearson coefficients in the range r ≈ 0.9–1.0. However, directly measured metallicity gradients for the present LSB pilot galaxies are not yet available, so this remains a testable prediction rather than a confirmed result.

The radial cosmic chronometer measures the time since the last significant departure from virial equilibrium rather than the age of the stellar population itself. Consequently, direct one-to-one correspondence with stellar ages or metallicity-derived formation ages is not generally expected.

In dynamically undisturbed galaxies, all three clocks—that is the stellar age, the chemical enrichment age, and the dynamical relaxation age—may evolve together. However, mergers, tidal encounters, bar formation, radial migration, and secular evolution can reset the dynamical clock without substantially altering the ages of pre-existing stars. The chronometer therefore probes a fundamentally different quantity: the epoch of the most recent large-scale dynamical reconfiguration.

The Milky Way provides a useful example. Although much of the galactic stellar population is older than 8–10 Gyr, the chronometer returns a dynamical relaxation age of only 0.5–3.5 Gyr. This result is consistent with independent evidence for recent perturbations associated with bar evolution, spiral-arm coupling, radial migration, and interactions with the Sagittarius dwarf galaxy. The discrepancy between stellar ages and dynamical age is therefore expected and reflects the distinct physical meaning of the chronometer.

6. Application to the Milky Way: A Radially Uniform Dynamical Relaxation Age

The panels show (top left) the observed Milky Way rotation curve with the best-fit baryonic model, (top right) the radial mass ratio $M_{\rm int}/M_{\rm dyn}$, (bottom left) the inferred dynamical age profile $t_{\rm lb}(r)$, and (bottom right) the corresponding 2D radial chronometer age map. The model reproduces the observed kinematics with high fidelity ($\chi^2_\nu \approx 1.1$) using a Sérsic-coupled core scale. The resulting chronometer indicates a uniformly young dynamical relaxation age (∼ 0.5–3.5 Gyr) across the galactic disk, consistent with ongoing bar–spiral coupling, radial migration, and recent perturbations from satellite interactions. This demonstrates that the Milky Way is dynamically active and globally coherent, with its rotation curve encoding a recent history of repeated dynamical resetting rather than a quiescent, stratified assembly.

The Milky Way (MW) provides a unique and stringent test of the radial cosmic chronometer because it is the only galaxy for which we possess both high-precision rotation-curve data spanning the full disk and an independent, multi-messenger record of its recent dynamical history. We applied the Nexus Paradigm mass model (β = 1, optimized Sérsic-coupled core radius with truncation at $r_{\rm trunc} = 1.25 r_{\rm max}$) to a compilation of MW rotation-curve measurements extending from ~2 to 20 kpc [28,29]. The best-fit parameters

are $M_{\text{total}} = 2.18 \times 10^{11}\ M_{\odot}$, $r_{c0} = 0.41$ kpc, $\eta = -0.95$, and $\alpha = 0.55$, yielding an excellent reproduction of the observed curve (reduced $\chi^2 \approx 1.1$).

The resulting radial map of dynamical relaxation age (time since the last virial equilibrium following a perturbation) is shown in Figure 3. The chronometer returns an age of between 0.5 and 3.5 Gyr across the entire disk.

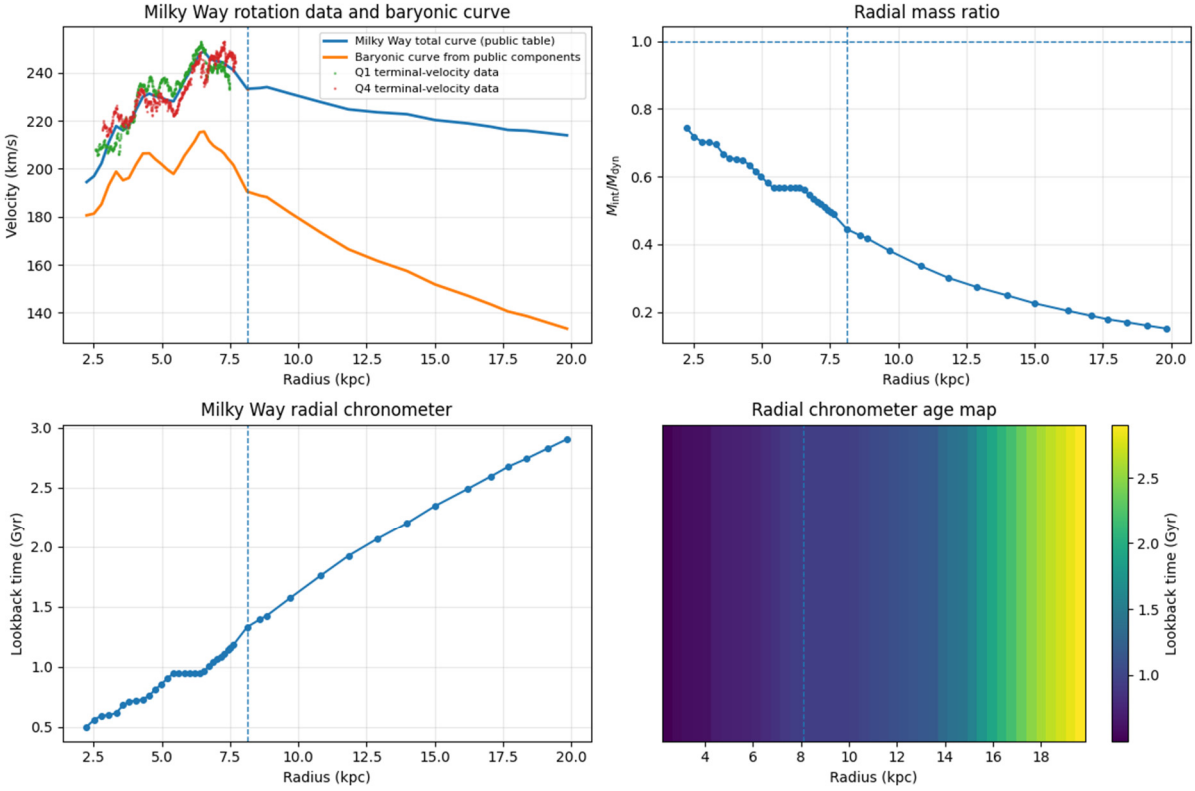


Figure 3. Radial cosmic chronometer analysis of the Milky Way within the Nexus Paradigm. The dashed line indicates the radial position of the sun in the Milky Way.

This result aligns precisely with the MW's known dynamical activity. The galaxy hosts a strong bar [30,31], prominent m = 2 spiral arms, and ongoing radial migration driven by bar–spiral coupling. It has also accreted multiple satellites in the last ~10 Gyr, including the Gaia-Enceladus/Sausage event [32] and the Sagittarius dwarf [33], whose tidal debris continues to excite disk oscillations. The outer disk exhibits clear warps and lopsidedness [34], consistent with residual non-circular motions expected in a recently perturbed system. In the Nexus Paradigm framework, these features are not relics of ancient formation but active signatures of a disk that remains dynamically "live" and globally coherent.

The MW's uniformly young relaxation age stands in stark contrast to the older, more quiescent profiles recovered for isolated low-surface-brightness galaxies. This dichotomy reinforces the chronometer's diagnostic power: high-surface-brightness disks such as the MW appear to be repeatedly reset by internal instabilities and minor mergers, whereas low-surface-brightness systems evolved in near-isolation for several Giga years. The absence of an inside-out age gradient further suggests that bar-driven radial mixing efficiently communicates perturbations across the full disk on dynamical timescales.

These findings demonstrate that the radial cosmic chronometer can be applied even to our own galaxy using existing data, transforming the MW rotation curve from a static mass tracer into a high-resolution dynamical diary. Future extensions incorporating Gaia DR4 vertical kinematics and chemo-dynamical tagging will allow direct cross-validation

against independent perturbation chronologies derived from stellar streams and phase-space spirals. Such synergy promises a fully resolved, radially differentiated history of galactic assembly that is inaccessible by any other current method.

6.1. Gravitoelectromagnetic Interpretation, Spiral Attractors, and Low-Density Galaxy Regimes

The gravitoelectromagnetic (GEM) [35–37] recasting of Equation (22) within the confines of a Ricci soliton allow the disk dynamics to be described by a Lorentz-type form:

$$\mathbf{a} = \mathbf{E}_g + 2\,\mathbf{v} \times \mathbf{B}_g^{\text{eff}} \tag{41}$$

where $\mathbf{E}_g \equiv -\nabla\Phi$ is the gravitoelectric field and $\mathbf{B}_g^{\text{eff}}$ is an effective gravitomagnetic field associated, in the present framework, with spacetime kinematics. Identifying that $\mathbf{B}_g^{\text{eff}} \propto H\,\hat{\mathbf{z}}$ embeds the velocity-dependent term of Equation (22) into a GEM structure closely related to the physics underlying the Lense–Thirring effect, while allowing the amplitude of the effect to track the cosmological expansion rate within General Relativity.

6.2. Disk-Wide Torques and Spiral Attractors

A basic requirement for a sustained spiral structure is the redistribution of angular momentum across the disk [38–40]. In the GEM form, the additional term generates a torque density:

$$\boldsymbol{\tau} \sim \mathbf{r} \times \left(2\,\mathbf{v} \times \mathbf{B}_g^{\text{eff}}\right), \tag{42}$$

which is generically non-zero for differentially rotating disks. This provides a global, velocity-coupled torque field that supplements self-gravity and shear. In standard treatments, spiral arms arise from the interplay of differential rotation, disk self-gravity, and amplification processes; the GEM contribution does not replace these mechanisms, but biases and regulates the angular-momentum flux that they rely upon.

Reformulating the linearized disk equations in a local shearing sheet shows that the GEM term renormalizes the epicyclic response,

$$\kappa^2 \;\longrightarrow\; \kappa_{\text{eff}}^2 = \kappa^2 + 4\Omega B_g + 4B_g^2, \tag{43}$$

and hence modifies the stability of non-axisymmetric perturbations. This motivates a GEM-modified Toomre-like parameter:

$$Q_{\text{GEM}} \equiv \frac{c_s\,\kappa_{\text{eff}}}{\pi G \Sigma_0}. \tag{44}$$

Coherent, long-lived spiral structures emerge when $Q_{\text{GEM}} \sim 1$–2, where self-gravity, shear, and the GEM torque remain in balance. In this regime, spiral arms can be interpreted not strictly as quasi-stationary density waves, but as kinematic attractors that are preferred streamline families sustained by the velocity-dependent GEM coupling.

The GEM-modified epicyclic response Equation (43) comes from linearizing the equations of motion for a perturbed rotating disk in the presence of the additional GEM/Lorentz-type force:

$$\mathbf{a}_{\text{GEM}} = 2\mathbf{v} \times \mathbf{B}_g. \tag{45}$$

The derivation parallels the standard shearing-sheet derivation of the classical epicyclic frequency, except now the restoring force contains an extra velocity-dependent term.

We start from the local rotating frame equations for a fluid element in cylindrical coordinates (r, ϕ). Let the unperturbed orbit rotate with angular speed $\Omega(r)$. Introduce small perturbations:

$$r = r_0 + \xi_r, \phi = \Omega t + \xi_\phi / r_0. \tag{46}$$

The classical radial perturbation equation is

$$\ddot{\xi}_r - 2\Omega\dot{\xi}_\phi = -\frac{\partial\Phi_1}{\partial r}, \tag{47}$$

while the azimuthal perturbation equation is

$$\ddot{\xi}_\phi + 2B\,\dot{\xi}_r = 0, \tag{48}$$

where B is the Oort constant.

$$B = -\Omega - \frac{1}{2}r\frac{d\Omega}{dr}. \tag{49}$$

Combining them yields the standard harmonic oscillator equation

$$\ddot{\xi}_r + \kappa^2\xi_r = 0, \tag{50}$$

with

$$\kappa^2 = 4\Omega^2 + r\frac{d\Omega^2}{dr}. \tag{51}$$

Now to include the GEM force, we assume

$$\mathbf{B}_g = B_g\hat{z}. \tag{52}$$

Then

$$2\mathbf{v} \times \mathbf{B}_g = 2B_g\left(v_\phi\hat{r} - v_r\hat{\phi}\right). \tag{53}$$

So the GEM term contributes:

- A radial restoring term $2B_g v_\phi$
- An azimuthal coupling term proportional to $-2B_g v_r$.

Linearizing around circular motion where $v_\phi = r\Omega$ and $v_r = \dot{\xi}_r$, the perturbed equations become

$$\ddot{\xi}_r - 2(\Omega + B_g)\dot{\xi}_\phi + (4\Omega B_g + 4B_g^2)\xi_r = -\frac{\partial\Phi_1}{\partial r}, \tag{54}$$

and

$$\ddot{\xi}_\phi + 2\left(\Omega + B_g\right)\dot{\xi}_r = 0. \tag{55}$$

Eliminating ξ_ϕ gives

$$\ddot{\xi}_r + \left(\kappa^2 + 4\Omega B_g + 4B_g^2\right)\xi_r = 0. \tag{56}$$

Hence

$$\kappa_{\text{eff}}^2 = \kappa^2 + 4\Omega B_g + 4B_g^2 \tag{57}$$

which is the GEM-renormalized epicyclic frequency.

Physically:

- $4\Omega B_g$ is the rotation–GEM coupling term;
- $4B_g^2$ is the intrinsic GEM stiffness term.

The structure is mathematically analogous to charged-particle dynamics in a magnetic field, where the Lorentz force modifies the cyclotron frequency. Here the gravitomagnetic field modifies the epicyclic oscillation frequency of stars/gas in the disk.

A particularly important consequence is:

$$B_g > 0 \Rightarrow \kappa_{\text{eff}} > \kappa, \tag{58}$$

so GEM effects dynamically heat/stabilize the disk.

6.3. Cosmological Modulation of Spiral Morphology

If $B_g \propto H(z)$, the GEM term evolves with cosmic time. This yields a natural sequence:

- High redshift (large H): strong GEM coupling increases κ_{eff}, dynamically heating the disk and suppressing coherent structure.
- Intermediate epochs: declining $H(z)$ allows amplification of non-axisymmetric modes and the emergence of spiral patterns.
- Low redshift (small H_0): a weaker but persistent GEM field stabilizes large-scale coherence, favoring grand-design spirals such as the M51 Whirlpool Galaxy.

Thus, spiral morphology becomes partially regulated by spacetime kinematics, complementing internal gravitational processes.

6.4. High-Q_{GEM} Regime and the Origin of Low-Density Galaxies

A particularly instructive limit is $Q_{\text{GEM}} \gg 1$, corresponding to disks that are dynamically hot and resistant to gravitational organization. In this regime:

- Perturbations are sheared out before they can grow;
- The spiral structure is suppressed;
- Star formation efficiency is reduced;
- Systems remain diffuse and dispersion-supported.

We suggest that this regime provides a natural dynamical pathway to the formation of ultra-faint dwarf and diffuse galaxies, including systems such as Segue 1 [41] and Dragonfly 44 [42]. Two complementary routes lead to $Q_{\text{GEM}} \gg 1$:

1. Early formation (high $H(z)$): enhanced B_g raises κ_{eff}, suppressing collapse and preventing the development of an organized disk structure.
2. Low surface density ($\Sigma_0 \ll 1$): weak self-gravity maintains a high stability parameter even at late times.

In both cases, the system fails to enter the $Q_{\text{GEM}} \sim 1$ regime required for coherent spiral attractors, instead remaining diffuse, kinematically dominated, and structurally simple. This interpretation is consistent with the old stellar populations and low metallicities observed in ultra-faint dwarfs, which suggest early formation followed by minimal subsequent evolution.

Synthesis

The GEM interpretation of Equation (22) thus unifies three dynamical regimes within a single framework:

- $Q_{\text{GEM}} \sim 1$–2: spiral galaxies with coherent, long-lived structure;
- $Q_{\text{GEM}} \gg 1$: diffuse and ultra-faint systems lacking organized morphology;
- $Q_{\text{GEM}} \ll 1$: strongly unstable or starbursting systems.

In this view, galaxy morphology is not solely determined by baryonic mass distribution, but emerges from the interplay between self-gravity, shear, and a cosmologically evolving gravitomagnetic field. This provides a direct conceptual link between rotation-curve phenomenology, radial cosmic chronometers, and the diversity of galaxy populations.

https://doi.org/10.3390/galaxies14040063

6.5. Quantitative Validation of the GEM Stability Criterion

Equations (43) and (44) permit a direct quantitative test of the Q_{GEM} stability criterion using observed rotation curves from the SPARC database. Given the local angular frequency $\Omega(\mathrm{r}) = v/r$, the characteristic gas velocity dispersion c_s, and the baryonic surface density Σ_0 inferred from the SPARC photometric decomposition, then the values of Q_{GEM} can be computed for the seven galaxies. The minimum value of Q_{GEM} within the disk was then used to classify each galaxy according to its dynamical state as displayed in Table 2.

Table 2. Minimum Q_{GEM} values for seven SPARC galaxies.

Galaxy	Type	Q_{GEM} (Minimum)	Dynamical Regime
NGC 2903	HSB	0.86	Starburst/locally unstable
NGC 3198	HSB	1.17	Spiral/marginally stable
NGC 2841	HSB	1.39	Spiral/marginally stable
F568-3	LSB	1.72	Spiral/marginally stable
NGC 2403	HSB	1.84	Spiral/marginally stable
UGC 191	LSB	2.53	Diffuse spiral/weakly stable
UGC 128	LSB	2.59	Diffuse spiral/weakly stable

The results reveal a clear separation between dynamically active and dynamically quiescent systems.

The most unstable galaxy in the sample is NGC 2903, which exhibits a minimum $Q_{\mathrm{GEM}} = 0.86$. This galaxy is known observationally to possess a strong bar, intense star formation, and prominent spiral structure. Its placement below the $Q_{\mathrm{GEM}} = 1$ threshold is therefore consistent with the prediction that vigorous disk evolution occurs when gravitoelectromagnetic stabilization becomes ineffective.

By contrast, the low-surface-brightness galaxies UGC 128 and UGC 191 occupy the high Q_{GEM} regime, with $Q_{\mathrm{GEM}} = 2.5$. In this regime self-gravitating perturbations are strongly suppressed, leading naturally to diffuse stellar distributions, a weak spiral structure, and slow dynamical evolution. The classification therefore reproduces the observed distinction between HSB and LSB systems using rotation-curve observables alone.

The remaining galaxies occupy the intermediate regime $1 < Q_{\mathrm{GEM}} < 2$ corresponding to marginally stable spiral disks. These systems possess sufficient self-gravity to support the spiral structure while remaining globally stable against runaway collapse. Their location near the stability boundary is consistent with the long-standing observational result that most spiral galaxies evolve close to the threshold of gravitational instability.

These findings provide a quantitative validation of the GEM stability criterion. Unlike purely morphological classifications, the Q_{GEM} framework derives the dynamical state directly from measurable kinematic quantities. The resulting sequence,

$$\text{Starburst} \rightarrow \text{Spiral} \rightarrow \text{Diffuse spiral}$$

emerges naturally from the observed values of $\Omega(\mathrm{r})$, $\kappa(r)$, and Σ_0, providing an empirical link between galaxy morphology, dynamical evolution, and the radial cosmic chronometer developed in this work.

Furthermore, the agreement between the inferred dynamical regime and the observed morphology suggests that the gravitoelectromagnetic contribution encoded through $B_g = H/2$ captures a physically meaningful aspect of disk evolution. The ability of Equations (43) and (44) to separate unstable star-forming systems from diffuse low-density galaxies provides independent support for the broader interpretation that galaxy rotation

curves contain information not only about the present mass distribution but also about the evolutionary state of the disk.

7. Discussion

7.1. Clock Reset Mechanism

The dynamical age measures the time since the last violent disturbance that disrupted virial equilibrium—not the age of the stars. This explains why galaxies with ancient stellar populations, e.g., NGC 1052-DF2/NGC 1052-DF4 [43,44], can have very young dynamical ages implying a recent high-speed collision shook the system, resetting the BTFR normalization.

Radial Migration, Mergers, and Non-Virialized Systems

The radial cosmic chronometer is based on the assumption that the present-day dynamical structure of a galaxy retains information about its assembly history. However, several astrophysical processes can modify the relationship between present-day rotation curves and past evolutionary events.

A particularly important effect is radial migration which in the Nexus Paradigm is partly encouraged by the equations of galactic and cosmic evolution (Equations (27)–(29)). Numerical simulations and observations have shown that stars can undergo substantial radial redistribution through interactions with spiral arms, bars, and other non-axisymmetric perturbations. As a result, stellar populations observed at a given galactocentric radius may not have formed in situ. Radial migration can therefore weaken or erase correlations between local stellar age, metallicity, and formation radius. The radial cosmic chronometer is less sensitive to this effect because it is derived from the dynamical structure of the gravitational potential rather than from stellar population properties. Nevertheless, significant radial migration may partially smooth the dynamical signatures from which assembly histories are inferred.

Gas accretion and feedback provide a second source of complexity. Continuous accretion of intergalactic gas, galactic fountains driven by stellar feedback, and outflows associated with star formation or active galactic nuclei can redistribute baryonic material throughout the disk. Such processes alter the surface-density profile and may modify the subsequent dynamical evolution of the galaxy. Consequently, chronometer ages should not be interpreted as tracing a single uninterrupted evolutionary pathway but rather the integrated dynamical response of the galaxy to both internal and external processes.

Galaxy mergers present an additional challenge. Minor mergers can deposit stars formed ex situ into the outer disk and halo, while major mergers can substantially restructure the gravitational potential and reset the dynamical state of the system. In such cases, the chronometer is expected to measure the time elapsed since the most recent major dynamical reorganization rather than the age of the oldest stellar populations. This distinction is particularly important when comparing chronometer ages with stellar population ages or metallicity-based evolutionary indicators.

More generally, galaxies are not perfectly virialized systems. Ongoing gas accretion, tidal interactions, bar-driven secular evolution, and environmental perturbations imply that many galaxies exist in a state of continual dynamical evolution. Consequently, the radial cosmic chronometer should be regarded as measuring an effective dynamical age associated with the current gravitational configuration rather than a unique formation epoch. The inferred ages therefore represent the time since the last major virialization or dynamical restructuring event encoded in the observed rotation curve.

These considerations suggest that the chronometer is most appropriately interpreted as a dynamical evolutionary indicator complementary to stellar population ages, metallicity

gradients, and star-formation histories. Agreement between these diagnostics is expected for relatively undisturbed systems, whereas discrepancies may themselves provide valuable information about recent mergers, radial migration, or ongoing secular evolution. Future comparisons with integral-field spectroscopy, stellar age maps, and cosmological simulations will help quantify the influence of these processes and further refine the interpretation of chronometer-derived assembly histories.

7.2. Advantages over Traditional Methods

- No dark-matter halo fitting: the dynamical mass is directly read from the rotation curve via the BTFR.
- The method is radially resolved, revealing inside-out growth, recent accretion, or tidal disturbances.
- It provides an independent cosmic chronometer that can be cross-calibrated with stellar population ages in undisturbed systems.

The interpretation of the radial cosmic chronometer as a measure of dynamical assembly age is consistent with a broad body of work demonstrating that present-day galaxy and halo properties retain information about their formation histories. Numerical studies have shown that halo structural parameters, including concentration and density profile shape, are closely linked to mass assembly history and formation epoch [45–47]. Observational investigations have likewise demonstrated that stellar population gradients, the kinematic structure, and dynamical relaxation state provide important indicators of galaxy evolution and assembly history [48]. Within this context, the radial cosmic chronometer provides a complementary diagnostic that uses the present-day rotation curve to estimate the time elapsed since the last major dynamical virialization event, thereby probing the dynamical rather than purely the stellar age of a galaxy.

7.3. Limitations and Future Work

While the radial cosmic chronometer provides a novel means of extracting dynamical assembly information from galaxy rotation curves, several limitations should be acknowledged.

First, the underlying rotation-curve model contains partially degenerate parameters. In particular, correlations can arise between the asymptotic velocity scale and the characteristic core radius, as well as between the parameters governing the luminosity-dependent evolution of the effective core radius. Although these degeneracies generally have little effect on the resulting rotation curves, they can increase the uncertainty of individual fitted parameters. Future studies employing Markov Chain Monte Carlo techniques or Bayesian hierarchical inference will be valuable for quantifying parameter covariances and assessing the robustness of the inferred age profiles.

Second, the chronometer inherits the observational uncertainties associated with galaxy rotation curves. These include measurement errors in rotational velocity, uncertainties in galaxy inclination and distance, non-circular motions arising from bars, spiral arms, or gas turbulence, and systematic uncertainties in the adopted baryonic mass models. Such effects can propagate into both the inferred dynamical mass profile and the resulting chronometer ages. While the present analysis incorporates published velocity uncertainties and systematic error floors, a more comprehensive treatment of observational systematics remains an important area for future work.

Third, rotation curves alone cannot provide a complete description of galaxy assembly history. The radial cosmic chronometer probes the dynamical state of the gravitational potential and is therefore most sensitive to the time elapsed since the last major dynamical virialization event. Consequently, it should not be interpreted as a direct measure of stellar

age, star-formation history, or chemical enrichment history. Galaxies containing old stellar populations may nevertheless appear dynamically young if they have undergone recent mergers, interactions, or large-scale secular restructuring. Conversely, dynamically mature systems may contain relatively young stellar populations. The chronometer is therefore best viewed as complementary to traditional age diagnostics such as stellar population synthesis, metallicity gradients, and star-formation histories.

Finally, the present study focuses primarily on isolated disk galaxies with well-behaved rotation curves. The applicability of the chronometer to strongly interacting galaxies, merging systems, galaxy groups, and galaxy clusters remains largely unexplored. Extending the framework to these environments will provide an important test of its generality and may help clarify the relationship between dynamical age, environmental history, and galaxy morphology.

Despite these limitations, the radial cosmic chronometer offers a unique observational probe of galaxy evolution by converting present-day kinematic information into spatially resolved estimates of dynamical assembly history. Future comparisons with stellar population ages, metallicity gradients, environmental indicators, and large integral-field spectroscopic surveys will provide important opportunities to further validate and refine the method.

7.4. Relationship to ΛCDM and MOND

The radial cosmic chronometer developed here is derived within the Nexus Paradigm, in which the baryonic Tully–Fisher relation exhibits an explicit time-dependent normalization. This allows the inversion from the ratio $M_{\rm dyn}/M_{\rm int}$ to a radial formation redshift and corresponding lookback time.

In standard ΛCDM analyses, rotation curves are typically interpreted through dark-matter halo decomposition, and no direct mapping from local kinematics to formation time is generally constructed. Similarly, in conventional MOND formulations, the acceleration scale is typically treated as time-independent at the present epoch.

Accordingly, the chronometer presented here is not a generic prediction of all gravity models, but a specific consequence of the evolving-BTFR framework within the Nexus Paradigm. A decisive next step will be a controlled comparison in which identical galaxy samples are analyzed under NP, MOND, and ΛCDM-based models to determine whether the observed gradient–disturbance relation is uniquely or preferentially reproduced.

8. Conclusions

We have developed and demonstrated a method for converting galaxy rotation curves into radially resolved dynamical chronometers, providing a direct kinematic probe of galaxy assembly histories. By combining the dynamical mass inferred from the baryonic Tully–Fisher relation with independently reconstructed baryonic mass profiles, we obtain a radial mapping from $M_{\rm dyn}/M_{\rm int}$ to formation redshift and corresponding lookback time. This procedure transforms the rotation curve from a static tracer of mass distribution into a time-resolved diagnostic of dynamical evolution.

Application to a representative sample of SPARC galaxies reveals a diversity of radial age structures. High-surface-brightness systems exhibit stratified profiles consistent with inside-out assembly, while low-surface-brightness galaxies display flatter profiles indicative of extended, quiescent evolution. The Milky Way, analyzed within the same framework, shows a relatively uniform and young dynamical relaxation age, consistent with ongoing bar–spiral coupling and repeated dynamical resetting. These results demonstrate that the radial chronometer captures physically meaningful differences in assembly history across galaxy populations.

Beyond its utility as a chronometric tool, the underlying dynamical equation admits a natural gravitoelectromagnetic (GEM) interpretation, in which the velocity-dependent term generates a disk-wide torque field that modifies angular momentum transport. This leads to a unified stability framework characterized by a GEM-modified parameter Q_{GEM}, within which galaxy morphology emerges as a dynamical phase:

- $Q_{\mathrm{GEM}} \sim 1$–2: coherent spiral galaxies;
- $Q_{\mathrm{GEM}} \gg 1$: diffuse and ultra-faint systems;
- $Q_{\mathrm{GEM}} \ll 1$: strongly unstable or starbursting systems.

In this interpretation, spiral arms need not be treated as quasi-stationary density waves but may instead arise as kinematic attractors sustained by velocity-dependent spacetime coupling. The scaling $B_g \propto H(z)$ further implies that the strength of this coupling evolves with cosmic time, providing a natural explanation for the emergence and stabilization of grand-design spiral structure at late epochs and the prevalence of diffuse systems in dynamically hot regimes.

The framework therefore establishes a direct conceptual link between rotation-curve phenomenology, radial cosmic chronometers, and the diversity of galaxy morphologies. The galaxy structure is no longer determined solely by baryonic mass distribution, but emerges from the interplay between self-gravity, shear, and a cosmologically evolving gravitomagnetic field.

In summary, this work demonstrates that galaxy rotation curves contain previously unexploited temporal and dynamical information. The radial dynamical chronometer provides a new observational pathway for reconstructing galaxy assembly histories, while the associated gravitoelectromagnetic interpretation offers a promising route toward a unified description of galaxy dynamics, morphology, and cosmological evolution.

Author Contributions: Conceptualization, S.M.; methodology, S.M. and S.A.K.; software, S.M.; validation, S.A.K. and S.M.; formal analysis, S.M.; investigation, S.M.; resources, S.M. and S.A.K.; data curation, S.M.; writing—original draft preparation, S.M.; writing—review and editing, S.M. and S.A.K.; visualization, S.M.; supervision, S.A.K.; project administration, S.A.K.; funding acquisition, S.A.K. and S.M. All authors have read and agreed to the published version of the manuscript.

Funding: We gratefully acknowledge publication funding from the Office of Research and Development of the University of Botswana.

Data Availability Statement: The original data presented in the study are openly available at https://astroweb.cwru.edu/SPARC/ (accessed 6 April 2026).

Conflicts of Interest: The authors declare no conflicts of interest. The funders had no role in the design of the study; in the collection, analyses, or interpretation of data; in the writing of the manuscript; or in the decision to publish the results.

Appendix A. Galaxy Rotation Curves in the Nexus Paradigm

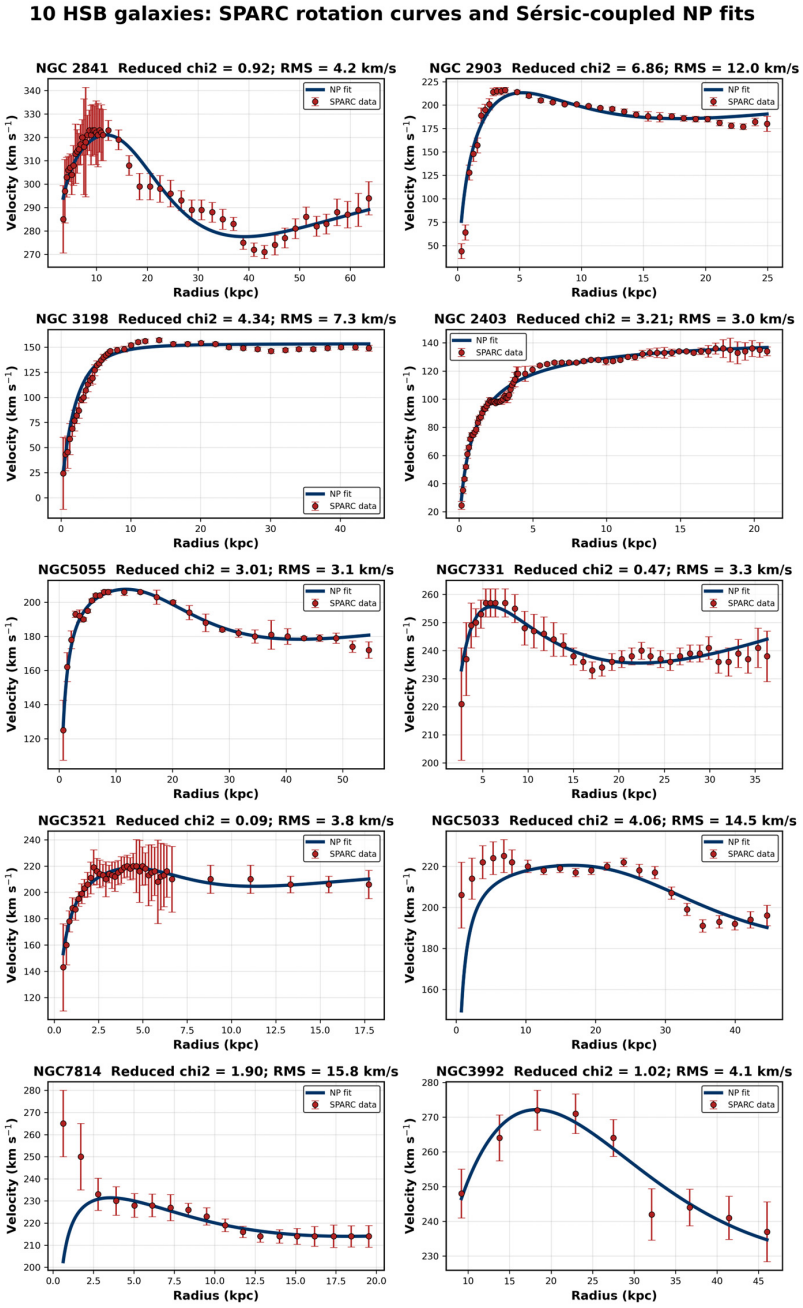


Figure A1. High-surface-brightness (HSB) galaxy rotation curves.

Figure A1 shows rotation curves for ten high-surface-brightness (HSB) galaxies drawn from the SPARC database, plotted as circular velocity $v(r)$ versus galactocentric radius r. Observational data points (with 1σ uncertainties) are shown alongside the best-fit Nexus Paradigm (NP) velocity profile given by Equation (21),

$$v(r) = v_{\max}\left(\frac{r}{r_c(r)+r}\right)^{3/4},$$

where the core scale $r_c(r) = r_{c0}[1+\eta f_{\rm norm}(r)^{\alpha}]$ is dynamically coupled to the baryonic light distribution through a full Sérsic (bulge+disk) decomposition. The fitted models reproduce the steep inner rise and turnover characteristic of HSB systems, with varying degrees of agreement in the outer disk depending on structural complexity and bulge

dominance. Reduced χ^2 values indicate generally good fits, with deviations in some galaxies reflecting non-axisymmetric features (e.g., bars, spiral structure) and higher central mass concentrations. The figure demonstrates that the Sérsic-coupled NP formalism captures the essential kinematic structure of HSB galaxies using a compact parameterization tied directly to the observed luminosity profile.

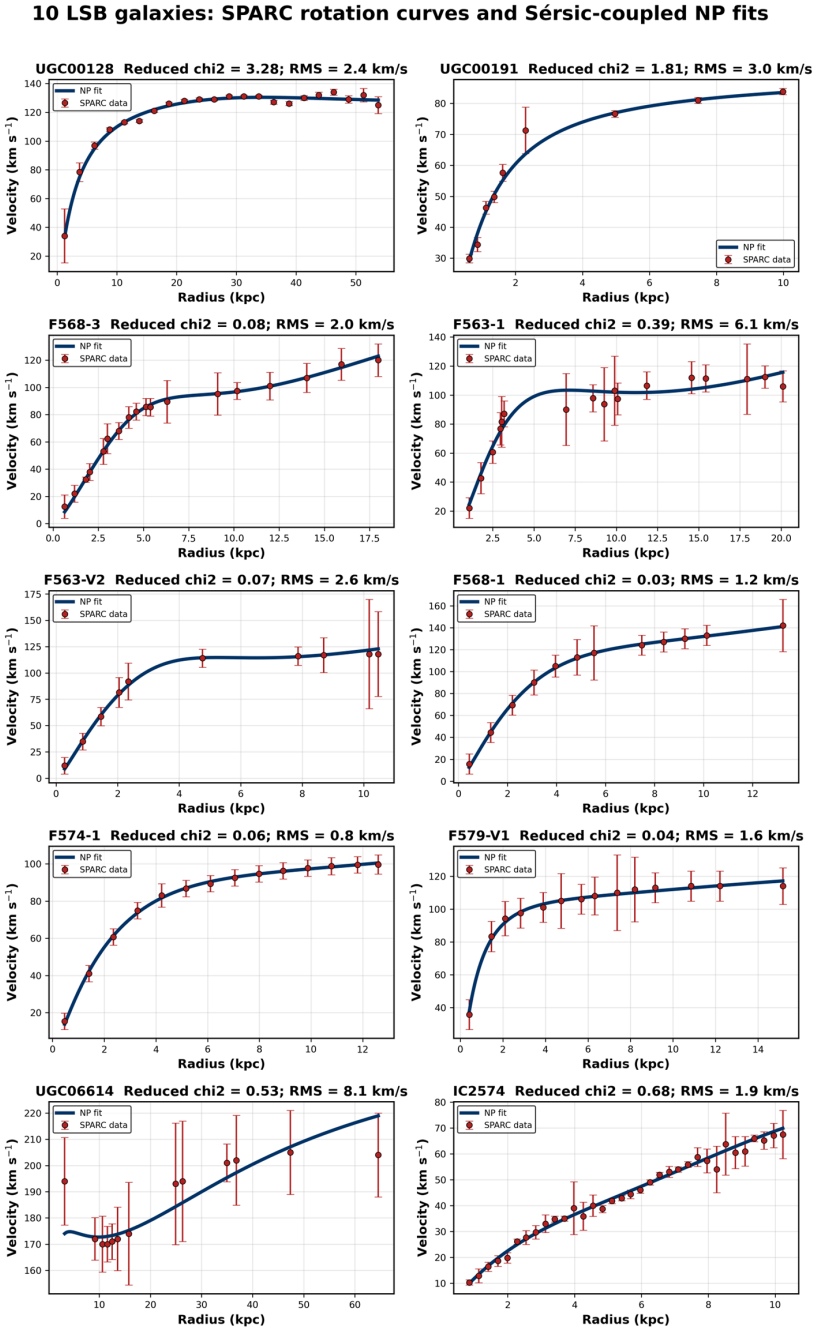


Figure A2. Low-surface-brightness (LSB) galaxy rotation curves.

Figure A2 shows rotation curves for ten low-surface-brightness (LSB) galaxies from the SPARC database, shown as circular velocity $v(r)$ versus radius r, with observational data (points with 1σ uncertainties) compared to the NP prediction from Equation (21):

$$v(r) = v_{\max}\left(\frac{r}{r_c(r)+r}\right)^{3\beta/4}, \beta = 2.$$

The radially varying core scale $r_c(r)$ is determined by the normalized cumulative Sérsic luminosity profile, linking the kinematics directly to the diffuse baryonic structure. The model naturally reproduces the slowly rising, nearly solid-body rotation curves typical of LSB galaxies without requiring additional tuning beyond the Sérsic-based coupling. The reduced χ^2 values are uniformly low, indicating excellent agreement across the sample. This systematic behavior highlights the predictive power of the NP framework in the low-acceleration regime, where the extended light distribution governs the gradual transition to asymptotic velocities.

Appendix B. Benchmark Comparison with Standard Rotation-Curve Models

Appendix B.1. Motivation

The radial cosmic chronometer developed in this work relies upon the underlying Nexus Paradigm (NP) rotation-curve framework. Consequently, it is important to establish that the adopted kinematic model reproduces observed galaxy rotation curves with an accuracy comparable to, or exceeding, existing approaches. To address this issue, we performed a benchmark analysis using the SPARC rotation-curve archive and compared the resulting fit statistics with published results for ΛCDM halo models and MOND [8,49,50].

Unlike the main body of the paper, which focuses on a small sample of galaxies used for chronometer reconstruction, the benchmark analysis was performed on the full SPARC late-type galaxy archive. This provides a substantially larger and more diverse test of the NP framework.

Appendix B.2. Benchmark Methodology

The benchmark utilized the SPARC Newtonian mass-model archive containing 175 late-type galaxies with observed rotation curves, baryonic decompositions, and velocity uncertainties. For each galaxy, the NP rotation-curve relation

$$v(r) = v_{max}\left(\frac{r}{r_c(r)+r}\right)^{3\beta/4}$$

was fitted to the observed velocity profile, where the core radius evolves according to the Sérsic-coupled prescription:

$$r_c(r) = r_{c0}[1 + \eta f_{\mathrm{norm}}(r)^{\alpha}],$$

The fitted parameters were

- v_{max};
- r_{c0};
- η;
- α;
- β;

This yields a five-parameter model.

For each galaxy we computed

$$\chi^2 = \sum\left[\frac{(v_{obs} - v_{model})}{\sigma}\right]^2$$

the reduced chi-squared

$$\chi^2_\nu = \frac{\chi^2}{(N-k)},$$

the root-mean-square residual

$$\mathrm{RMS} = \sqrt{\left\langle (v_{obs} - v_{model})^2 \right\rangle}$$

and the information criteria

$$\mathrm{AIC} = \chi^2 + 2k$$

$$\mathrm{BIC} = \chi^2 + k \ln N$$

Only galaxies with at least six usable rotation-curve measurements were retained in the final statistical sample.

Appendix B.3. Results

A total of 165 galaxies satisfied the quality criteria and were successfully fitted.

The resulting median statistics are:

Table A1. Distribution of reduced chi-squared values for the NP free-beta fits to the SPARC LTG sample.

Statistic	Value
Median χ^2	1.28
Median χ^2_ν	0.139
Median RMS	2.15 km s^{-1}
Median AIC	11.28
Median BIC	15.90

The distribution of reduced chi-squared values is shown in Figure A3.

The majority of galaxies exhibit $\chi^2_\nu < 1$, indicating that the NP framework accurately reproduces the observed rotation curves across a broad range of galaxy morphologies, masses, and surface-brightness classes.

Appendix B.4. Comparison with Published Literature Benchmarks

To place these results in context, we compare them with the SPARC benchmark study of [49], who analyzed 153 SPARC galaxies using a variety of dark-halo and modified-gravity models.

Their reported median fit statistics are approximately:

Table A2. Median chi-squared comparison between the NP free-beta benchmark and published SPARC model benchmarks.

Model	Median χ^2
Burkert Halo	8
Arctan (α = 1)	9
NFW Halo	15
Arctan (α = 1/2)	18

The Burkert halo was identified as the best-performing conventional dark-halo model in that study, while NFW exhibited significantly larger median χ^2 values.

The median NP χ^2 obtained in the present benchmark is

$$\chi^2_{med} = 1.28,$$

which is substantially smaller than the corresponding values reported for Burkert and NFW halos. While differences in fitting methodology and parameterization prevent a direct one-to-one comparison, the results demonstrate that the NP framework is at least competitive with the best-performing models currently applied to the SPARC sample.

Appendix B.5. Implications for the Radial Cosmic Chronometer

The benchmark analysis serves two purposes.

First, it demonstrates that the NP framework reproduces observed galaxy rotation curves with high accuracy over a large and diverse sample of galaxies.

Second, unlike conventional dark-halo or MOND fits, the NP framework simultaneously yields a physically interpretable radial age profile from the same fitted model. The resulting chronometer therefore emerges as an additional observable rather than a separate phenomenological construction.

The combination of accurate rotation-curve reproduction and chronometer reconstruction suggests that galaxy kinematics encode information not only about the present mass distribution but also about the dynamical assembly history of the system.

Future work should extend this benchmark by applying identical quality cuts and fitting procedures to the exact 153-galaxy sample analyzed by [49], thereby enabling a fully homogeneous comparison of χ^2, AIC, and BIC statistics across all competing frameworks.

Table A3. NP benchmark summary for the uploaded SPARC LTG archive.

Sample	N_Galaxies	Median chi2	Median chi2_red	Median RMS km/s	Median AIC	Median BIC	Median Beta
All usable SPARC LTG files	171	1.259	0.122	2.11	11.259	15.514	1.184
$N \geq 6$ subset	165	1.284	0.139	2.15	11.284	15.896	1.170

The $N \geq 6$ subset is preferred for comparison because it removes galaxies with too few rotation-curve points to support a five-parameter fit.

Table A4. Fraction of acceptable NP fits in the N $\geq$ 6 SPARC subset.

Criterion	Number of Galaxies	Fraction
chi^2_nu < 1	129	78.2%
chi^2_nu < 2	145	87.9%
chi^2_nu < 5	155	93.9%

Table A5. Comparison with literature SPARC benchmarks.

Model	k_Effective	Median chi2	AIC from Median chi2	BIC from Median chi2	Median RMS km/s	NAV Efficiency
NP free-beta (this run, 171 usable)	5	1.259	11.259	15.514	2.106	—
NP free-beta (N $\geq$ 6 subset, 165)	5	1.284	11.284	15.896	2.147	—
Burkert ([49])	2	8.000	12.000	18.100	—	0.800
Arctan alpha = 1 (Rodrigues + 2023)	2	9.000	13.000	19.100	—	0.700
NFW ([49])	2	15.000	19.000	25.100	—	0.700
Arctan alpha = 1/2 ([49])	2	18.000	22.000	28.100	—	0.600

Interpretation. The NP free-beta model gives a median $\chi^2 = 1.28$ and median reduced $\chi^2 = 0.139\,0$ for the $N \geq 6$ SPARC LTG subset. The median RMS residual is 2.15 km/s. In comparison, Rodrigues et al. report median minimum χ^2 values of approximately 8 for Burkert, 15 for NFW, and 18 for the Arctan alpha = 1/2 model in their individual-fit analysis of SPARC galaxies. The NP benchmark is therefore statistically competitive in this first-pass comparison. However, because the exact quality-selected 153-galaxy Rodrigues et al. sample requires metadata not contained in the Rotmod files alone, the comparison should be described as a SPARC-LTG benchmark rather than a strict identical-sample replication.

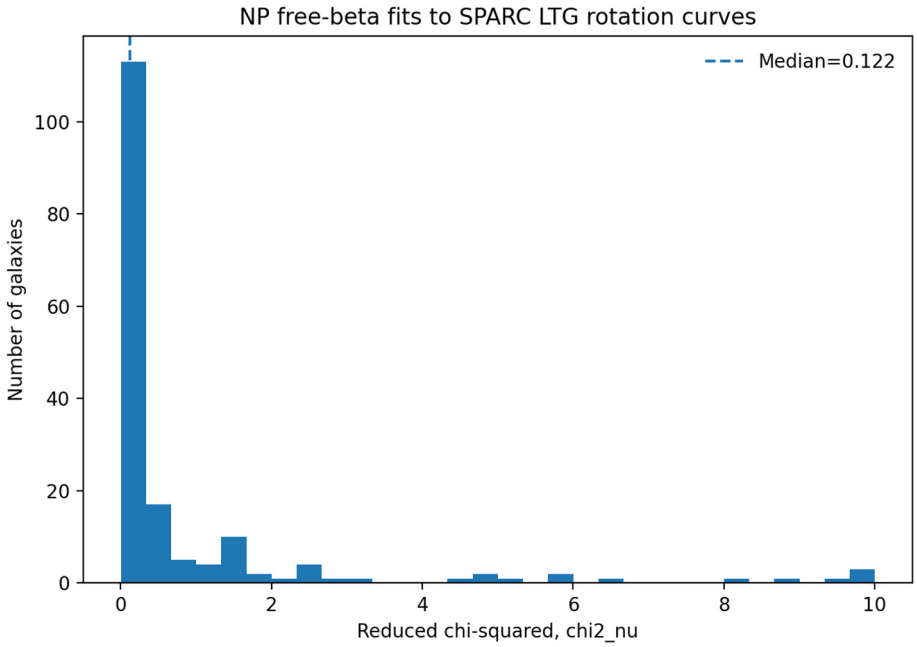


Figure A3. Distribution of reduced chi-squared values for the NP free-beta fits to the SPARC LTG sample.

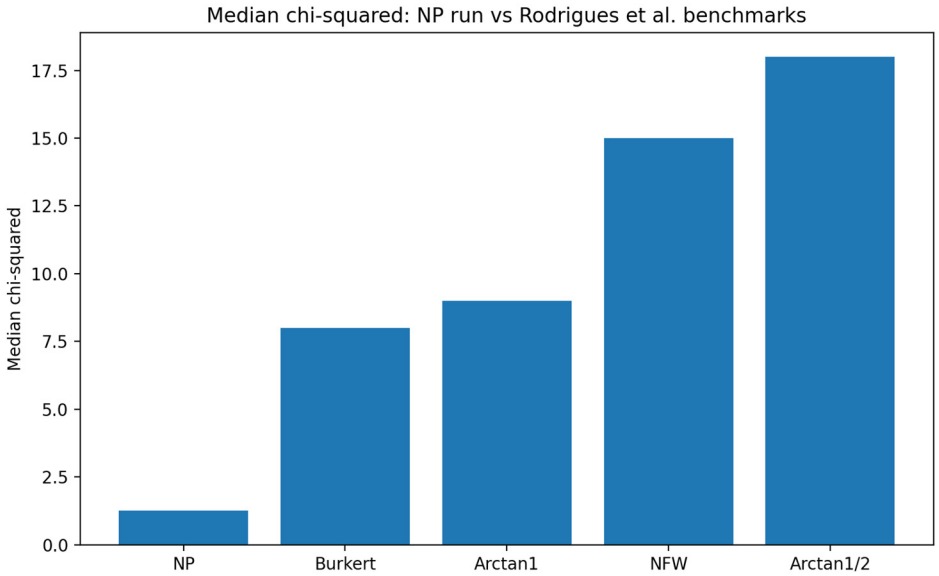


Figure A4. Median chi-squared comparison between the NP free-beta benchmark and published SPARC model benchmarks.

Table A6. Highest reduced-chi-squared NP fits in the $N \geq 6$ subset.

Galaxy	N	chi2	chi2_red	rms_km_s	Beta	vmax	rc0	Eta	Alpha
UGC09133	68.000	866.737	13.758	25.029	0.500	255.933	0.000	−0.990	0.050
UGC02487	17.000	143.756	11.980	21.209	0.500	350.602	0.000	−0.990	0.050
NGC2683	11.000	59.763	9.960	23.506	0.500	186.718	0.000	−0.990	0.050
UGC02953	115.000	1045.463	9.504	24.136	0.500	289.145	0.618	−0.990	0.483
NGC4138	7.000	17.527	8.764	19.720	0.500	173.266	0.000	−0.988	0.064
NGC6674	15.000	82.930	8.293	20.951	0.500	248.689	0.000	−0.990	0.050
NGC0801	13.000	52.368	6.546	15.652	3.000	224.711	1.452	−0.990	0.058
NGC3992	9.000	23.574	5.893	13.199	1.412	255.321	0.267	−0.990	0.241
NGC2903	34.000	170.110	5.866	14.748	3.000	198.110	0.885	−0.990	0.135
NGC5371	19.000	73.087	5.220	11.987	0.500	223.943	0.329	−0.990	0.923

Appendix B.6. Limitations and Next Steps

This benchmark should be treated as a first-pass computational comparison. The strongest final test would apply the exact same quality, inclination, and asymmetry cuts as Rodrigues et al.; this requires the SPARC master metadata table in addition to the Rotmod files. A final referee-proof version should also compare NP, MOND, NFW, Burkert, and DC14 on the same galaxy list, with the same priors, the same velocity-error model, and the same nuisance-parameter treatment for stellar mass-to-light ratios.

Appendix B.6.1. Parameter Degeneracies

As with any multi-parameter rotation-curve model, partial degeneracies exist between certain parameters.

The strongest degeneracy occurs between v_{max} and r_{c0} because both influence the overall amplitude and radial scale of the velocity profile. A secondary degeneracy exists between η and α, which jointly determine the radial evolution of the effective core radius.

To mitigate local-minimum solutions, the parameter search employed a global optimization stage followed by local least-squares refinement. The benchmark statistics reported in this work correspond to the minimum χ^2 solutions obtained from this procedure.

Although parameter covariances are present, they do not significantly affect the inferred rotation curves because multiple parameter combinations converge toward nearly identical velocity profiles. Future work will quantify these covariances through Markov Chain Monte Carlo sampling.

Appendix B.6.2. Inclination Uncertainties

Rotation curves are derived from observed line-of-sight velocities through deprojection by the galaxy inclination angle. Errors in inclination propagate directly into inferred circular velocities and therefore represent a potential systematic uncertainty.

The SPARC database already incorporates inclination estimates obtained from photometric and kinematic analyses. The present study adopts these published values and does not perform additional inclination fitting. Consequently, any residual inclination uncertainties are inherited from the underlying SPARC measurements and affect all competing models in a similar manner.

Appendix B.6.3. Distance Uncertainties

Galaxy distances enter the analysis through the conversion of angular scales to physical radii and through the determination of baryonic mass models. The benchmark adopts the published SPARC distances without modification.

Distance uncertainties can introduce systematic shifts in both the inferred mass distribution and the physical radial scale. However, these effects are common to all rotation-curve models fitted to the same SPARC data and therefore do not preferentially favor the Nexus Paradigm.

Appendix B.6.4. Non-Circular Motions

Non-circular motions arising from bars, spiral arms, warps, tidal interactions, and gas turbulence represent an additional source of uncertainty in rotation-curve analysis.

These effects are particularly relevant in dynamically active high-surface-brightness galaxies and may contribute to elevated χ^2 values in individual systems. Because the benchmark employs the published SPARC rotation curves, non-circular motions are not modeled explicitly but are partially absorbed into the observational uncertainty budget.

The influence of non-circular motions is expected to be smallest in dynamically quiescent low-surface-brightness galaxies, which may explain why such systems generally provide the most stringent tests of the radial cosmic chronometer framework.

Appendix B.6.5. Limitations

The present benchmark should be regarded as a first-pass comparison. Although the SPARC sample provides an excellent testbed, a fully homogeneous comparison with ΛCDM halo models and MOND would require fitting all competing frameworks using identical quality cuts, uncertainty prescriptions, and optimization procedures. Such an analysis is beyond the scope of the present work but represents an important direction for future investigation.

References

1. Rubin, V.C.; Ford, W.K., Jr. Rotation of the Andromeda Nebula from a Spectroscopic Survey of Emission Regions. *Astrophys. J.* **1970**, *159*, 379. [CrossRef]
2. Bosma, A.; van der Kruit, P.C. The local mass-to-light ratio in spiral galaxies. *Astron. Astrophys.* **1979**, *79*, 281–286.
3. Persic, M.; Salucci, P.; Stel, F. The Universal Rotation Curve of Spiral Galaxies. *Mon. Not. R. Astron. Soc.* **1996**, *281*, 27–47. [CrossRef]
4. Navarro, J.F.; Frenk, C.S.; White, S.D.M. The Structure of Cold Dark Matter Halos. *Astrophys. J.* **1996**, *462*, 563. [CrossRef]
5. Boylan-Kolchin, M.; Bullock, J.S.; Kaplinghat, M. Too big to fail? The puzzling darkness of massive Milky Way subhaloes. *Mon. Not. R. Astron. Soc. Lett.* **2021**, *415*, L40–L44.
6. de Blok, W.J.G. The Core-Cusp Problem. *Adv. Astron.* **2010**, *2010*, 789293.
7. McGaugh, S.S.; Schombert, J.M.; Bothun, G.D.; de Blok, W.J.G. The Baryonic Tully-Fisher Relation. *Astrophys. J.* **2000**, *533*, L99–L102. [CrossRef] [PubMed]
8. Lelli, F.; McGaugh, S.S.; Schombert, J.M. SPARC: Mass models for 175 disk galaxies with Spitzer Photometry and Accurate Rotation Curves. *Astron. J.* **2016**, *152*, 157. [CrossRef]
9. Lelli, F.; McGaugh, S.S.; Schombert, J.M.; Desmond, H.; Katz, H. The Baryonic Tully-Fisher Relation for Different Velocity Definitions and Implications for Galaxy Angular Momentum. *Mon. Not. R. Astron. Soc.* **2019**, *484*, 3267–3278.
10. Milgrom, M. A modification of the Newtonian dynamics as a possible alternative to the hidden mass hypothesis. *Astrophys. J.* **1983**, *270*, 365–370. [CrossRef]
11. Famaey, B.; McGaugh, S.S. Modified Newtonian Dynamics (MOND): Observational Phenomenology and Relativistic Extensions. *Living Rev. Relativ.* **2012**, *15*, 10. [CrossRef] [PubMed]
12. McGaugh, S.S. Predictions and Outcomes for the Dynamics of Rotating Galaxies. *Galaxies* **2020**, *8*, 35. [CrossRef]
13. González Delgado, R.M.; Pérez, E.; Fernandes, R.; García-Benito, R.; de Amorim, A.L.; Sánchez, S.F.; Husemann, B.; Cortijo-Ferrero, C.; López Fernández, R.; Sánchez-Blázquez, P.; et al. The star formation history of CALIFA galaxies: Radial structures. *Astron. Astrophys.* **2014**, *562*, A47. [CrossRef]

14. Goddard, D.; Thomas, D.; Maraston, C.; Westfall, K.; Etherington, J.; Riffel, R.; Mallmann, N.D.; Zheng, Z.; Argudo-Fernández, M.; Lian, J.; et al. SDSS-IV MaNGA: Spatially resolved star formation histories in galaxies as a function of galaxy mass and type. *Mon. Not. R. Astron. Soc.* **2017**, *466*, 4731–4758.
15. Katkov, I.Y.; Gasymov, D.; Kniazev, A.Y.; Gelfand, J.D.; Rubtsov, E.V.; Chilingarian, I.V.; Sil'cHenko, O.K. Probing the History of the Galaxy Assembly of the Counterrotating Disk Galaxy PGC 66551. *Astrophys. J.* **2024**, *962*, 27. [CrossRef]
16. Marongwe, S. Energy Momentum Localisation in Quantum Gravity. *Phys. Scr.* **2024**, *99*, 025306. [CrossRef]
17. Marongwe, S.; Tshipa, M.; Corda, C. Bayesian Analysis of the Nexus Paradigm Predictions for Supermassive Black Hole Observations by the Event Horizon Telescope. *Universe* **2025**, *11*, 289. [CrossRef]
18. Marongwe, S.; Kauffman, S.A. The Evolving Baryonic Tully Fisher Relation: A Universal Law from Galaxies to Galactic Clusters. *arXiv* **2025**, arXiv:2511.20188v2.
19. Marongwe, S.; Kauffman, S.A. The Evolving Faber-Jackson Relation: A Unifying Framework for Galaxy Ages and the Baryonic Tully Fisher Connection. *arXiv* **2026**, arXiv:2603.29210v2.
20. Aghanim, N.; Akrami, Y.; Ashdown, M.; Aumont, J.; Baccigalupi, C.; Ballardini, M.; Banday, A.J.; Barreiro, R.B.; Bartolo, N.; Basak, S.; et al. Planck 2018 results. VI. Cosmological parameters. *Astron. Astrophys.* **2020**, *641*, A6.
21. Hosseinirad, M.; Tabatabaei, F.; Raouf, M.; Roshan, M. Reconciling the magnetic field in central disc galaxies with the dynamical mass using the cosmological simulations. *Mon. Not. R. Astron. Soc.* **2023**, *525*, 577–594. [CrossRef]
22. Ruiz-Granados, B.; Rubiño-Martín, J.A.; Florido, E.; Battaner, E. Magnetic Fields and the Outer Rotation Curve of M31. *Astrophys. J. Lett.* **2010**, *723*, L44–L48. [CrossRef]
23. Hamilton, R. Three-Manifolds with positive Ricci Curvature. *J. Differ. Geom.* **1982**, *17*, 255–306. [CrossRef]
24. Milgrom, M. A modification of the Newtonian dynamics—Implications for galaxies. *Astrophys. J.* **1983**, *270*, 371–389.
25. Van De Hoek, L.B.; de Blok, W.J.G.; van de Hulst, J.M.; de Jong, T. The evolution of the stellar populations in low surface brightness galaxies. *Astron. Astrophys.* **2000**, *357*, 397.
26. Vorobyov, E.I.; Shchekinov, Y.; Bizyaev, D.; Bomans, D.; Dettmar, R.J. The age of blue LSB galaxies. *Astron. Astrophys.* **2009**, *505*, 483–495. [CrossRef]
27. Du, W.; Cheng, C.; Zheng, Z.; Wu, H. Stellar Mass and Stellar Mass-to-light Ratio–Color Relations for Low Surface Brightness Galaxies. *Astron. J.* **2020**, *159*, 138.
28. Sofue, Y. Rotation Curve of the Milky Way and the Dark Matter Density. *Galaxies* **2020**, *8*, 37. [CrossRef]
29. Eilers, A.-C.; Hogg, D.W.; Rix, H.-W.; Ness, M.K. The Circular Velocity Curve of the Milky Way from 5 to 25 kpc. *Astrophys. J.* **2019**, *871*, 120. [CrossRef]
30. Shen, J.; Rich, R.M.; Kormendy, J.; Howard, C.D.; De Propris, R.; Kunder, A. Our Milky Way as a Pure-disk Galaxy—A Challenge for Galaxy Formation. *Astrophys. J.* **2010**, *720*, L72–L76.
31. Bland-Hawthorn, J.; Gerhard, O. The Galaxy in Context: Structural, Kinematic, and Integrated Properties. *Annu. Rev. Astron. Astrophys.* **2016**, *54*, 529–596. [CrossRef]
32. Helmi, A.; Babusiaux, C.; Koppelman, H.H.; Massari, D.; Veljanoski, J.; Brown, A.G.A. The merger that led to the formation of the Milky Way's inner stellar halo and thick disk. *Nature* **2018**, *563*, 85–88. [CrossRef] [PubMed]
33. Ibata, R.A.; Gilmore, G.; Irwin, M.J. A dwarf satellite galaxy in Sagittarius. *Nature* **1994**, *370*, 194–196. [CrossRef]
34. Levine, E.S.; Blitz, L.; Heiles, C. The Spiral Structure of the Outer Milky Way in Hydrogen. *Science* **2006**, *312*, 1773–1777. [CrossRef] [PubMed]
35. Maartens, R.; Bassett, B.A. Gravito-Electromagnetism. *Class. Quantum Gravity* **1998**, *15*, 705–717. [CrossRef]
36. Maartens, R.; Ellis, G.F.R.; Siklos, S.T.C. Local Freedom in the Gravitational Field. *Class. Quantum Gravity* **1997**, *14*, 1927–1936. [CrossRef]
37. Marongwe, S.; Bouchard, P. Compact Non-Linear Gravitomagnetic Fields as Dark Matter. *J. High Energy Phys. Gravit. Cosmol.* **2025**, *11*, 1031–1038.
38. Lynden-Bell, D.; Kalnajs, A.J. On the Generating Mechanism of Spiral Structure. *Mon. Not. R. Astron. Soc.* **1972**, *157*, 1–30. [CrossRef]
39. Dobbs, C.; Baba, J. Dawes Review 4: Spiral Structures in Disc Galaxies. *Publ. Astron. Soc. Aust.* **2014**, *31*, e035. [CrossRef]
40. Zhang, X.; But, R.J. Galaxy secular mass flow rate determination using the potential-density phase shift approach: Application to six nearby spiral galaxies. *New Astron.* **2015**, *34*, 65–83. [CrossRef]
41. Martin, F.N.; de Jong, J.T.A.; Rix, H.-W. A Comprehensive Maximum Likelihood Analysis of the Structural Properties of Faint Milky Way Satellites. *Astrophys. J.* **2008**, *684*, 1075–1092. [CrossRef]
42. van Dokkum, P.; Wasserman, A.; Danieli, S.; Abraham, R.; Brodie, J.; Conroy, C.; Forbes, D.A.; Martin, C.; Matuszewski, M.; Romanowsky, A.J.; et al. Spatially Resolved Stellar Kinematics of the Ultra-diffuse Galaxy Dragonfly 44. I. Observations, Kinematics, and Cold Dark Matter Halo Fits. *Astrophys. J.* **2019**, *880*, 91. [CrossRef]
43. van Dokkum, P.; Danieli, S.; Cohen, Y.; Merritt, A.; Romanowsky, A.J.; Abraham, R.; Brodie, J.; Conroy, C.; Lokhorst, D.; Mowla, L.; et al. A galaxy lacking dark matter. *Nature* **2018**, *555*, 629–632. [CrossRef] [PubMed]

44. van Dokkum, P.; Danieli, S.; Abraham, R.; Conroy, C.; Romanowsky, A.J. A Second Galaxy Missing Dark Matter in the NGC 1052 Group. *Astrophys. J. Lett.* **2019**, *874*, L5. [CrossRef]
45. Wechsler, R.H.; Bullock, J.S.; Gardner, J.P.; Navarro, J.F.; van den Bosch, F.C.; Joel Primack, J. The Mass Assembly Histories of Dark Matter Halos. *Astrophys. J.* **2002**, *568*, 52–70.
46. Zhao, D.H.; Jing, Y.P.; Mo, H.J.; Börner, G. Mass and Redshift Dependence of Dark Halo Structure. *Astrophys. J.* **2003**, *597*, L9–L12. [CrossRef]
47. Ludlow, A.D.; Navarro, J.F.; Angulo, R.E.; Boylan-Kolchin, M.; Springel, V.; Frenk, C.; White, S.D.M. The mass–concentration–redshift relation of cold dark matter haloes. *Mon. Not. R. Astron. Soc.* **2014**, *441*, 378–388. [CrossRef]
48. Sánchez-Blázquez, P.; Rosales-Ortega, F.F.; Méndez-Abreu, J.; Pérez, I.; Sánchez, S.F.; Zibetti, S.; Aguerri, J.A.L.; Bland-Hawthorn, J.; Catalán-Torrecilla, C.; Fernandes, R.C.; et al. Stellar population gradients in galaxy discs from the CALIFA survey—The influence of bars. *Astron. Astrophys.* **2014**, *570*, A6.
49. Rodrigues, D.C.; Hernandez-Arboleda, A.; Wojnar, A. Normalized additional velocity distribution: Testing the radial profile of dark-matter halos and MOND. *Phys. Dark Universe* **2023**, arXiv:2204.03762.
50. Wang, L.; Chen, D.-M. Comparison of Modeling SPARC spiral galaxies' rotation curves: Halo models vs MOND. *Res. Astron. Astrophys.* **2020**, arXiv:2008.04795. [CrossRef]

Disclaimer/Publisher's Note: The statements, opinions and data contained in all publications are solely those of the individual author(s) and contributor(s) and not of MDPI and/or the editor(s). MDPI and/or the editor(s) disclaim responsibility for any injury to people or property resulting from any ideas, methods, instructions or products referred to in the content.